

2
3 **Article Info**

4 *Article history:*

5 Received 6 April 2016

6 Received in revised form 24 August 2016

7 Accepted 27 August 2016

8 Available online 5 October 2016

9 Editor: M. Frank

10
11
12
13 **ASTRONOMICAL CONSTRAINTS ON THE DURATION OF THE EARLY**
14 **JURASSIC PLIENSBACHIAN STAGE AND GLOBAL CLIMATIC**
15 **FLUCTUATIONS**

16
17 MICHA RUHL¹, STEPHEN P. HESSELBO^{1,2}, LINDA HINNOV³, HUGH C. JENKYN¹, WEIMU
18 XU¹, JAMES B. RIDING⁴, MARISA STORM¹, DANIEL MINISINI⁵, CLEMENS V. ULLMANN²,
19 MELANIE J. LENG^{4,6}
20

21 ¹ Department of Earth Sciences, University of Oxford, South Parks Road, Oxford OX1 3AN, UK

22 ² Camborne School of Mines and Environment and Sustainability Institute, University of Exeter, Penryn
23 Campus, Penryn, Cornwall, TR10 9FE, UK

24 ³ Department of Atmospheric, Oceanic and Earth Sciences, George Mason University, Fairfax Campus,
25 4400 University Drive, Fairfax, VA 22030, Virginia, USA

26 ⁴ British Geological Survey, Keyworth, Nottingham NG12 5GG, UK

27 ⁵ Shell Exploration and Production Incorporated, Shell Houston Technology Center, 3333 Highway 6
28 South, Houston, TX 77082, Texas, USA

29 ⁶ School of Geography, University of Nottingham, University Park, Nottingham NG7 2RD, UK
30
31

32 **Keywords:** *astrochronology, carbon-cycle, cyclostratigraphy, Early Jurassic, Pliensbachian, strontium*
33 *isotopes*
34

35 **ABSTRACT**

36 The Early Jurassic was marked by multiple periods of major global climatic and
37 palaeoceanographic change, biotic turnover and perturbed global geochemical
38 cycles, commonly linked to large igneous province volcanism. This epoch was
39 also characterized by the initial break-up of the super-continent Pangaea and the
40 opening and formation of shallow-marine basins and ocean gateways, the timing
41 of which are poorly constrained. Here, we show that the Pliensbachian Stage and
42 the Sinemurian–Pliensbachian global carbon-cycle perturbation (marked by a
43 negative shift in $\delta^{13}\text{C}$ of 2–4‰), have respective durations of ~8.7 and ~2 Myr. We
44 astronomically tune the floating Pliensbachian time scale to the 405 Kyr
45 eccentricity solution (La2010d), and propose a revised Early Jurassic time scale
46 with a significantly shortened Sinemurian Stage duration of 6.9 ± 0.4 Myr. When
47 calibrated against the new time scale, the existing Pliensbachian seawater
48 $^{87}\text{Sr}/^{86}\text{Sr}$ record shows relatively stable values during the first ~2 Myr of the
49 Pliensbachian, superimposed on the long-term Early Jurassic decline in $^{87}\text{Sr}/^{86}\text{Sr}$.
50 This plateau in $^{87}\text{Sr}/^{86}\text{Sr}$ values coincides with the Sinemurian–Pliensbachian
51 boundary carbon-cycle perturbation. It is possibly linked to a late phase of
52 Central Atlantic Magmatic Province (CAMP) volcanism that induced enhanced
53 global weathering of continental crustal materials, leading to an elevated
54 radiogenic strontium flux to the global ocean.

55
56
57
58
59
60
61
62
63
64
65
66
67
68
69
70
71
72
73
74
75
76
77
78
79
80
81
82
83
84
85
86
87
88
89
90
91
92
93
94
95
96
97
98
99
100
101
102
103
104
105

[1] INTRODUCTION

The Early Jurassic (201.4–174.1 Ma) is distinguished by the end-Triassic mass extinction and global warming event, climatic cooling in the Late Pliensbachian and subsequent greenhouse warming in the Early Toarcian (McElwain et al., 1999; Hesselbo et al., 2002; Ruhl et al., 2011; Gradstein et al., 2012; Wotzlaw et al., 2014; Gomez et al., 2015; Korte et al., 2015). Continental rifting and the break-up of Pangaea in the Early Jurassic led to the formation of continental and marine rift basins, which acted as major sites of organic carbon burial and led to the generation of hydrocarbon source rocks (Fleet et al., 1987; Olsen, 1997). The equatorial Tethys Ocean was connected in the Early Jurassic (Sinemurian) to Eastern Panthalassa via the Hispanic Corridor and to the high-latitude Boreal realm via the Viking Corridor, likely initiating changes in (global) ocean currents and planetary heat distribution (Figure 1; Porter et al., 2013; Korte et al., 2015).

The Early Toarcian in particular was set apart by the global Toarcian Oceanic Anoxic Event (T-OAE), with possibly the largest exogenic carbon-cycle perturbation in the Mesozoic, and associated perturbations in other global geochemical cycles, palaeoclimate and the palaeoenvironment, linked to emplacement of a large igneous province (LIP) in the Karoo-Ferrar region (Jenkyns, 2010; Burgess et al., 2015; Percival et al., 2015). The Early Jurassic was also marked by multiple somewhat smaller scale fluctuations in the global exogenic carbon cycle (Riding et al., 2013; Jenkyns and Weedon, 2013), shifts between climatic warming and cooling on regional and global scales (Korte et al., 2009; Korte and Hesselbo, 2011; Korte et al., 2015), marine and continental extinction and origination events (Close et al., 2015), and fluctuations in regional and global sea-level (Hallam, 1997; Hesselbo et al., 2004, 2008). The age, rate of change, and duration of these events are, however, poorly constrained and their inter-relationships only crudely appreciated.

Here, we determine the age and duration of the Early Jurassic Pliensbachian Stage and ammonite zones and subzones in the hemipelagic marine sedimentary record of the Mochras Farm (Llanbedr) Borehole from west Wales (Cardigan Bay Basin). The Mochras Borehole represents ~1300 m of possibly the most continuously deposited and stratigraphically expanded Lower Jurassic sedimentary archive known (Figure 2; Hesselbo et al., 2013). High-resolution (sub-precession scale) element concentration data from this cored material are used to construct a floating astronomical time scale for the Early Jurassic Pliensbachian Stage. Combined with published astrochronological and radiometric constraints on the age of the Rhaetian–Hettangian (Triassic–Jurassic) and Pliensbachian–Toarcian Stage boundaries, and astrochronological constraints on the duration of the Hettangian and Toarcian Stages, we calculate the duration and age of the Pliensbachian Stage and its constituent zones. With these data, we then assess the duration and rate of change of the Sinemurian–Pliensbachian climatic and global carbon-cycle perturbations and the Late Pliensbachian climatic cooling cycles, and assess the rate of change of Pliensbachian seawater $^{87}\text{Sr}/^{86}\text{Sr}$.

[2] THE MOCHRAS FARM (LLANBEDR) BOREHOLE

The Mochras Farm (Llanbedr) Borehole, hereafter referred to as Mochras, was drilled in 1968–1970 on the west coast of Wales (52°48'32" N, 4°08'44" W; Figure 1; Woodland, 1971; Dobson and Whittington, 1987; Hesselbo et al., 2013; Copestake and Johnson, 2014). The borehole yielded, unexpectedly, a ~1.3 km-thick (601.83–1906.78 m below surface), biostratigraphically complete succession of calcareous mudstone and clay-rich limestone, representing almost the complete Early Jurassic, an interval representing some 27 Myr of geological time.

The Early Jurassic age sedimentary record in the Mochras core is more than twice

106 as thick as any other UK core or coastal outcrop, and it is over four times more
107 expanded than the well-studied Sancerre–Couy core from the Paris Basin, France (Figure
108 2; Tappin et al., 1994; Hesselbo et al., 2013; Boulila et al., 2014). The Hettangian and
109 Sinemurian part of the Mochras core was largely broken up for ammonite
110 biostratigraphy; hence only limited continuous core is preserved for these stages.
111 Continuous core slabs are, however, preserved for the Pliensbachian and Toarcian parts
112 of Mochras (Hesselbo et al., 2013).

113

114 [3] BIO- AND CHEMOSTRATIGRAPHY

115 Biostratigraphical zones, combined with high-resolution geochemical proxy records,
116 provide the primary means for global correlation of Lower Jurassic marine and terrestrial
117 sedimentary archives. The Pliensbachian Stage in northwest Europe is subdivided into
118 five ammonite zones (and 15 ammonite subzones), which are all present and recognized
119 in the Mochras core (Ivimey-Cook, 1971; Page, 2003; Copestake and Johnson 2014). In
120 this paper, these are referred to as zones and subzones, and are named by the index
121 species name (e.g. *margaritatus* zone). Foraminifers provide further biostratigraphical
122 constraints, and allow detailed correlation to records elsewhere (Copestake and Johnson,
123 2014).

124 The Pliensbachian is further marked by perturbations of global geochemical
125 cycles and climate. A 2–4‰ negative shift in the carbon-isotope composition ($\delta^{13}\text{C}$) of
126 skeletal (belemnite) calcite, bulk shallow-water carbonate, and organic matter is
127 recognized at the Sinemurian–Pliensbachian boundary at Robin Hood’s Bay (Yorkshire,
128 UK), the Central Apennines and Trento Platform (Italy), in Portugal and Germany, and
129 in the Mochras core (Jenkyns et al., 2002; Morettini et al., 2002; van de Schootbrugge et
130 al., 2005; Woodfine et al., 2008; Korte and Hesselbo, 2011; Franceschi et al., 2014). This
131 negative carbon-isotope excursion (CIE) likely represents a global carbon-cycle
132 perturbation and associated climatic change, and allows detailed stratigraphical
133 correlation, potentially at a resolution equivalent to, or even significantly higher than,
134 ammonite zones. The Late Pliensbachian was marked by a major positive shift, of up to
135 5‰, in the $\delta^{13}\text{C}$ of wood ($\delta^{13}\text{C}_{\text{WOOD}}$), and up to 3‰ in the $\delta^{13}\text{C}$ of organic matter
136 ($\delta^{13}\text{C}_{\text{TOC}}$; TOC: Total Organic Carbon) (Figure 7; Suan et al., 2010; Korte & Hesselbo,
137 2011; Silva et al., 2011), reflecting enrichment of ^{13}C in the coupled ocean-atmosphere
138 carbon pool, and thus a perturbation of the global carbon cycle. This carbon-cycle
139 perturbation determined from the upper *margaritatus* zone, correlates with regionally
140 identified sea-level fluctuations and associated changes in shallow-marine $\delta^{18}\text{O}_{\text{CALCITE}}$,
141 possibly reflecting climatic cooling cycles under conditions of massive carbon burial, with
142 an enhanced flux of organic matter from the ocean-atmosphere system to the
143 sedimentary carbon pool (Korte and Hesselbo, 2011). Alternatively, regional cooling may
144 have resulted from an early phase of obstruction of the Viking Corridor, leading to
145 decreased seawater temperatures across northwest Europe (Korte et al., 2015). The
146 observed Pliensbachian perturbations in global geochemical cycles allow for detailed
147 high-resolution stratigraphical correlation between geographically separated sedimentary
148 archives from both the marine and terrestrial realms.

149

150 [4] ANALYTICAL METHODS

151 High-resolution (10–15 cm) elemental concentrations (e.g. Ca, Fe, Ti) were obtained by
152 hand-held X-ray fluorescence (XRF) analyses on the slabbed archive half of the Mochras
153 core, from the Upper Sinemurian *ruricostatum* zone to the Lower Toarcian *tenuicostatum*
154 zone (1284.08–861.32 m). Rock-Eval analysis, providing Total Organic Carbon (TOC)
155 content, Hydrogen Index (HI) values and % Mineral Carbon, was performed on ~50 mg
156 of homogenized sample, with the Rock-Eval VI unit from Vinci Technologies, at the

157 department of Earth Sciences, University of Oxford. Analysis of $\delta^{13}\text{C}_{\text{TOC}}$ was performed
158 on decarbonated and homogenized Late Pliensbachian age outcrop samples from
159 Staithes (Yorkshire, UK), utilising ammonite biostratigraphy for correlation to the
160 Mochras core (Figure 7). Detailed methodology and data quality control are described in
161 the Supplementary Online Materials.

162

163 [5] RESULTS AND DISCUSSION

164 [5.1] SEDIMENTARY RHYTHMS IN THE PLIENSBACHIAN OF MOCHRAS

165 The Pliensbachian in the Mochras core shows metre-scale lithological couplets of pale
166 grey limestone and dark brown to grey, locally faintly laminated, mudstone, with
167 individual couplets commonly showing gradual transitions between these end-members
168 (Figure 3). The lithological expression of these couplets does, however, vary, in some
169 cases being represented by calcareous mudstone (commonly also more silty) alternating
170 with locally darker, shaly mudstone. These primary lithological cycles occur throughout
171 the Pliensbachian in the Mochras core and vary in thickness between ~ 30 cm (e.g. latest
172 Pliensbachian) and ~ 90 cm (e.g. Early Pliensbachian), with individual carbonate beds
173 measuring 20–40 cm (reduced to 5–20 cm in the Late Pliensbachian) (Figures 3, 4). The
174 lithological couplets are especially pronounced at the Sinemurian–Pliensbachian
175 transition (base *jamesoni* zone) and the top *ibex* to base *margaritatus* zones where they
176 comprise carbonate-poor mudstone with moderate organic-matter content (TOC: ~ 0.9 –
177 2.1%) and carbonate-rich mudstone or limestone (CaCO_3 : ~ 10 – 65%) with reduced
178 organic-matter content (Figures 3, 4; Supplementary Figure 2).

179 Individual lithological couplets are generally symmetrical in nature, with little
180 indication of depositional hiatus or scouring (Figure 3). The more organic-rich lithology
181 is commonly dark grey and faintly laminated on a millimetre scale, particularly in the
182 lowermost Pliensbachian part of the core, whereas the more carbonate-rich lithology is
183 commonly thoroughly bioturbated (Figure 3). Thin-section analysis shows evidence for
184 early diagenetic processes, such as calcite replacement and cementation (Supplementary
185 Figure 3), possibly resulting from the degradation of organic matter and the associated
186 reduction of sulfate, as evidenced by the occurrence of pyrite framboids. However, we
187 exclude the possibility that the lithological couplets are solely related to diagenesis, and
188 interpret them as depositional in origin, as supported by the burrow mottling, with dark-
189 pale and pale-dark mixing of primary sediments (cf. Hallam, 1986). Furthermore,
190 fluctuations in HI values of the bulk sedimentary organic matter closely match the
191 observed variations in CaCO_3 , suggesting a climatic control on periodic fluctuations in
192 the supply of organic and inorganic matter to the seabed (Supplementary Figure 2),
193 similar to that observed for the Upper Jurassic Kimmeridge Clay Formation at
194 Kimmeridge Bay (UK) and the Lower Jurassic Blue Lias Formation in southern England
195 (Weedon, 1985; Waterhouse, 1999; Weedon et al., 1999; Clemence et al., 2010; Ruhl et
196 al., 2010). Alternatively, observed drops in HI values may have resulted from the
197 oxidative removal of marine algal organic matter in better-oxygenated conditions in the
198 water column and/or sedimentary pore space.

199 Lithological couplets of similar character have also been observed for coeval
200 Pliensbachian successions in other marine basins across the UK (e.g. Sellwood, 1970,
201 1972; van Buchem and McCave, 1989; van Buchem et al., 1992, 1994; Hesselbo and
202 Jenkyns 1995; Weedon and Jenkyns, 1999). For example, lithological changes in the
203 Mochras core closely resemble the time-equivalent Belemnite Marl Member (Charmouth
204 Mudstone Formation) in outcrops on the Dorset coast, southern England, where
205 individual beds and distinct calcareous mudstone-shale couplets are laterally continuous
206 for over 2 km (Hesselbo and Jenkyns, 1995; Weedon & Jenkyns, 1999), suggesting
207 chronostratigraphical significance and a stable allogenic forcing mechanism, likely to be

208 high-frequency climate change. The latest Sinemurian and Pliensbachian sedimentary
209 sequence in the Mochras core also shows similar periodic alternations in lithology relative
210 to the coeval shallow-marine Redcar Mudstone Formation at Robin Hood's Bay,
211 although these latter sediments are characterized by silty to very fine sandy mudstone
212 beds alternating with silty mudstone and shale, with common levels of concretionary
213 siderite, and which were interpreted to originate from changes in storm frequency (van
214 Buchem & McCave, 1989; van Buchem et al., 1992, 1994; Hesselbo and Jenkyns 1995;
215 van Buchem and Knox, 1998).

216

217 [5.2] MILANKOVITCH-CONTROLLED SEDIMENTARY PERIODICITIES IN 218 THE PLIENSBACHIAN OF THE MOCHRAS CORE

219 The observed decimetre- to metre-scale amplitudinal change in calcium concentration
220 determined by XRF directly reflects the observed lithological couplets (in CaCO_3) and is
221 especially prominent around the Sinemurian–Pliensbachian boundary (*ruricostatum* and
222 *jamesoni* zones) and in the late Pliensbachian *margaritatus* zone (Figures 3, 4), illustrating a
223 strong modulation by long-term periodicities. Iron (Fe) and titanium (Ti) concentrations
224 in the Mochras core also fluctuate strongly and both are largely negatively correlated with
225 the calcium concentration (Figure 3), suggesting simple sedimentary carbonate dilution.
226 However, different climatic controls on detrital element supply or diagenetic element
227 enrichment may also have affected the carbonate-silicate balance. It is reasonable to
228 conclude that diagenesis exerted some control on the distribution of carbonate, likely
229 enhancing the primary lithological cyclicity inferred from sedimentary structures, trace
230 fossils, and other palaeontological characteristics outlined above. The observed
231 fluctuations in calcium concentrations therefore partly reflect relative changes in the
232 particulate carbonate flux, together with diagenetic effects that also have their origins in a
233 primary palaeoenvironmental cyclicity that may have occurred over Milankovitch time
234 scales.

235 The XRF-based Ca-concentration data series, combined with the stacked core-
236 photographs allow for the initial visual identification of calcareous beds and associated
237 lithological couplets. These lithological couplets are not evenly spaced, but occur in
238 bundles (E^1) of 4–5 sedimentary rhythms. Within a bundle the more calcareous beds
239 generally thicken up-section and become more pronounced, forming a weakly
240 asymmetric cycle (Figures 3, 4). Generally, four of these smaller bundles (E^1), each
241 consisting of 4–5 lithological couplets, occur in one super-bundle (E^2). The observed
242 couplets, bundles (E^1) and super-bundles (E^2) can generally be recognized throughout the
243 core, but vary in thickness, probably due to minor changes in sedimentation rate (Figure
244 4). The ratio between the thickness of the couplets, the bundles and the super-bundles is,
245 however, constant, consistent with a stable forcing mechanism, which we interpret as a
246 climatic control operating on Milankovitch frequencies.

247 The lithological couplets in the coeval Belemnite Marl Member in Dorset are
248 suggested to represent ~ 21 Kyr precession cyclicity (Weedon & Jenkyns, 1999).
249 Following this interpretation, we assign ~ 100 and ~ 405 Kyr eccentricity periodicities to
250 the visually defined bundles (E^1) and super-bundles (E^2) (Figures 3, 4). This procedure
251 allows for independent comparison to Milankovitch periodicities assigned from
252 subsequent spectral and multi-taper analyses. Some of the E^1 -bundles are, however,
253 marked by only two lithological couplets that are generally thicker and more carbonate-
254 rich, and which consistently occur only during the minimum between two E^2 -bundles
255 (Figure 4). Following the above, they may reflect a change from dominant eccentricity-
256 modulated precessional forcing to obliquity forcing.

257

258 [5.3] SPECTRAL & MULTI-TAPER ANALYSES

259 The XRF elemental data obtained from the Pliensbachian of the Mochras core were
260 manipulated to uniform sample spacing using linear interpolation. For spectral analyses,
261 the series were analyzed with the 3π multi-taper method (MTM) using the Astrochron
262 toolkit (Meyers, 2014; R Package for astrochronology, version 0.3.1), with robust red
263 noise models (Mann and Lees, 1996), and with AnalySeries 2.0.8 (Paillard et al., 1996).
264 Initial spectral analysis was performed with AnalySeries on a detrended data series (with
265 low band-pass filtering to remove periodicities >150 m). Dominant spectral components
266 (Supplementary Figure 4) were filtered from the data series, and compared to the visually
267 defined precession (lithological couplets) and long-term and short-term eccentricity
268 periodicities (Figure 4). The data-series in the depth domain was subsequently converted
269 into a time series, based on the observed and interpreted dominant ~ 405 Kyr eccentricity
270 cycle. Low-frequency band-pass filtering was then performed with Astrochron on the
271 raw-data time series to remove long-term trends. High-precision extraction of dominant
272 spectral components (Figure 5, Supplementary Figures 4, 5, 6), with long- and short-term
273 cycles of eccentricity, obliquity and precession, were subsequently extracted with Taner
274 bandpass filtering (Astrochron) and AnalySeries.

275 The MTM power spectrum estimates of the Ca-concentration in the depth
276 domain show dominance of the >150 m spectral peak (Supplementary Figure 4A).
277 Removal of this long-term trend by high band-pass filtering shows dominant spectral
278 components at ~ 1 , ~ 1.5 , ~ 2.5 , ~ 5.8 and ~ 24 m (Supplementary Figure 4B). Lithological
279 observations and visually described changes in Ca-concentrations show a pronounced
280 reduction in thickness of the observed lithological couplets, relative to the underlying
281 Pliensbachian strata, in the upper *margaritatus* and complete *spinatum* zones (Figure 4).
282 Individual couplets, however, continue to be spaced in the observed bundles (E^1) and
283 super-bundles (E^2), and lack any evidence of periodic hiatuses. The reduced thickness of
284 individual couplets, combined with the continued bundling, suggests an overall reduced
285 sedimentation rate in this part of the Mochras core.

286 Individual MTM power spectra for the uppermost *ruricostatum* to lower
287 *margaritatus* and the upper *margaritatus* to lowermost *tenuicostatum* zones (Supplementary
288 Figure 4C, 4D, respectively), show that dominant spectral components occur at different
289 frequencies, but with equal internal ratios suggesting a ~ 40 – 60% reduction in
290 sedimentation rate in the latest Pliensbachian and very earliest Toarcian (Supplementary
291 Figure 7). The ~ 1 and ~ 0.6 m spectral components in these intervals directly reflect the
292 observed primary sedimentary rhythms, recognized throughout the Pliensbachian of the
293 Mochras core (Figure 4). The observed dominant spectral peaks directly reflect the
294 visually ascribed individual lithological rhythms and bundles (E^1) and super-bundles (E^2)
295 in carbonate predominance, likely representing precession and short- and long-term
296 eccentricity. Using this interpretation, the sedimentary and geochemical time series of the
297 Mochras core can be converted from depth to age. The resulting floating astronomical
298 time scale for the Pliensbachian may also then be tuned to the proposed astronomical
299 solutions for this period (e.g. Laskar et al., 2011), using radiometric tie points.

300

301 [5.4] ASTRONOMICAL CONSTRAINTS ON THE DURATION OF THE 302 PLIENSBACHIAN STAGE AND AMMONITE ZONES

303 The base of the Pliensbachian is formally defined by a mudstone bed in the Pyritous
304 Shale Member (Redcar Mudstone Formation) at Robin Hood's Bay, Yorkshire, UK,
305 marked by the lowermost occurrence of the ammonite species *Bifericeras donovani*; with
306 additional stratigraphical markers including a narrow reversed-polarity magnetozone (at
307 the base of Si-Pl N) and a negative excursion in $\delta^{13}\text{C}$ (Hesselbo et al. 2000, Meister et al.,
308 2006; Korte and Hesselbo, 2011). The Pliensbachian Stage is conventionally divided into
309 the lower (Carixian) and upper (Domerian) substages and, at a higher resolution, into

310 ammonite zones. Some authors, e.g. Page (2004), prefer to treat ammonite-based
311 subdivisions as chronozones rather than biozones or zones but, given the absence of
312 corroboration of their time significance, we treat them here as conventional
313 biostratigraphical units. These are successions of sedimentary rock characterised by
314 specific fossil assemblages, and defined to be (closely) approximate in depositional age
315 and hence are characteristic of discrete time intervals.

316 The visual core observations and interpretations, combined with the spectral and
317 multi-taper analyses of geochemical records, together with the precise biostratigraphical
318 subdivision of the Mochras core, can be used to estimate the duration of Pliensbachian
319 ammonite zones. The precision of the estimates obtained for ammonite zone durations
320 depends on (1) the correct recognition of the dominant orbital signals, and (2) the
321 uncertainty of the precise position of the stratigraphical base of an ammonite zone in the
322 core. Here, we derive ammonite zone durations based on the observed 405 and ~100
323 Kyr forcing in the geochemical proxy-records. The stratigraphical occurrences of
324 ammonite genera identified in the Upper Sinemurian to Lower Toarcian sections of the
325 Mochras core, which are used to define the ammonite zones, is given in Supplementary
326 Figure 7.

327 Ammonite zones at Mochras are recognized on the basis of occurrences of
328 characteristic ammonite taxa within the core. Where ammonites are absent between the
329 highest occurrence of one stratigraphically significant taxon and the lowest occurrence of
330 another there is inevitably some uncertainty in the position of the biozone boundary
331 (such range uncertainty for Mochras is indicated diagrammatically in Supplementary
332 Figure 7 and Table 1). Given the above, resulting ammonite biozone durations are
333 estimated at ~2.7 Myr (*jamesoni*), ~1.8 Myr (*ibex*), ~0.4 Myr (*davoei*), ~2.4 Myr
334 (*margaritatus*) and ~1.4 Myr (*spinatum*), yielding a duration of the complete Pliensbachian
335 Stage of ~8.7 Myr (Figure 4; Table 1).

336 The durations estimated here for the *jamesoni* and *ibex* zones are significantly
337 longer than previous (minimum) estimates from the Belemnite Marl Member (Dorset)
338 and the Ironstone Shale (Yorkshire) (van Buchem et al., 1994; Weedon & Jenkyns, 1999).
339 The base and top of the Belemnite Marl Member (representing the base of the *jamesoni*
340 ammonite zone and the top of the *ibex* ammonite zone in the Dorset outcrops) are
341 marked by stratigraphic gaps (Hesselbo and Jenkyns, 1995; Weedon and Jenkyns, 1999),
342 likely explaining their shorter estimated durations. Equally, the Ironstone Shale in
343 Yorkshire shows strong evidence for condensation at the top of the *jamesoni* zone and
344 within the *ibex* zone (Hesselbo and Jenkyns 1995, 1998; van Buchem and Knox, 1998).

345 The likely underestimated durations of Early Pliensbachian ammonite zones
346 based on the Belemnite Marl Member sedimentary succession, are furthermore suggested
347 by time series analyses of the Mochras % Ca data imposed onto the Belemnite Marl
348 Member Early Pliensbachian time scale (Supplementary Figure 8), which shows spectral
349 peaks that have no correspondence to dominant astronomical frequencies as known
350 from the geological record and astronomical solutions (Supplementary Figure 8). The
351 new duration estimated here for the *davoei* zone is similar to an earlier proposed value
352 from Breggia Gorge in southern Switzerland, which was previously considered to be only
353 46% complete (Weedon, 1989). The latter was, however, based on the assumption that
354 Jurassic ammonite zones were ~1 Myr in duration and that only 22 of the expected 48
355 precession cycles could be recognized (Weedon, 1989). Given the similar duration
356 obtained for the *davoei* zone in the Mochras core, where no evidence for a hiatus,
357 condensation, or non-deposition has been observed, we argue that the *davoei* zone in the
358 Breggia Gorge section is probably complete. The estimated durations of the *margaritatus*
359 and *spinatum* zones are significantly longer, respectively 0.7 and 0.6 Myr, compared to
360 previous minimum estimates of Weedon (1989) and Weedon and Jenkyns (1999). Our

361 estimated duration of ~ 3.8 Myr for the combined *margaritatus*–*spinatum* ammonite zones
362 does, however, closely resemble previous estimates of ~ 3.96 Myr based on the assumed
363 rate of change of Early Jurassic seawater $^{87}\text{Sr}/^{86}\text{Sr}$ (McArthur et al., 2000). This does,
364 however, not infer that a linear change in $^{87}\text{Sr}/^{86}\text{Sr}$ likely occurred throughout the
365 Pliensbachian Stage. A recent estimate on the duration of the Pliensbachian Stage and
366 ammonite zones, with a stage duration of 8.1 Myr, does a-priori assume such linear
367 change for all, but the *jamesoni* zones (McArthur et al., 2016). Such assumption is not
368 necessarily correct, as the rate of change in the $^{87}\text{Sr}/^{86}\text{Sr}$ ratio of seawater can adjust on
369 multiple time-scales in response to a change in global climate and associated continental
370 (silicate) weathering rates, with a change in the flux of radiogenic $^{87}\text{Sr}/^{86}\text{Sr}$ to the global
371 oceans, relative to the dominant long-term unradiogenic marine hydrothermal/basalt
372 weathering Sr flux (see also section 5.7).

373

374 [5.5] TOWARDS AN ABSOLUTE TIME SCALE FOR THE EARLY JURASSIC 375 HETTANGIAN TO PLIENSBACHIAN STAGES

376 Zircon U-Pb radiometric dating of the earliest Central Atlantic Magmatic Province
377 (CAMP) flood basalts in eastern North America anchor the end-Triassic mass extinction
378 at 201.56 ± 0.02 Ma, and volcanoclastic material in the Pucara Basin of Peru, indicates an
379 age of 201.51 ± 0.15 Ma for the same event (Schoene et al., 2010; Blackburn et al., 2013;
380 Wotzlaw et al., 2014). The age of the Triassic–Jurassic boundary is radiometrically
381 constrained at 201.36 ± 0.17 Ma in the Pucara Basin (Schaltegger et al., 2008; Schoene et
382 al., 2010; Wotzlaw et al., 2014) and astrochronologically constrained at 201.42 ± 0.02 Ma
383 in the Newark/Hartford succession (Blackburn et al., 2013).

384 The duration of the Hettangian Stage has been previously estimated by
385 cyclostratigraphy at $> \sim 1.29$ Myr from the relatively incomplete marine Blue Lias
386 Formation succession in Dorset and Devon, SW England, or at ~ 2.86 Myr based on an
387 assumed constant linear Early Jurassic decrease in seawater $^{87}\text{Sr}/^{86}\text{Sr}$ ratios (Weedon and
388 Jenkyns, 1999). More recent estimates for this stage suggest a duration of ~ 1.7 – 1.9 Myr,
389 based on the astronomical interpretation of periodically occurring laminated black shales
390 and systematic fluctuations in organic and inorganic geochemical proxy records in the
391 relatively expanded Blue Lias Formation of Somerset, SW England (Ruhl et al., 2010;
392 Hüsing et al., 2014). This duration is further supported by palaeomagnetic correlation to
393 the Geomagnetic Polarity Time Scale (GPTS) of the Newark Basin, USA (Hüsing et al.,
394 2014), and a $199.43 (\pm 0.10)$ Ma $^{238}\text{U}/^{206}\text{Pb}$ age for the earliest Sinemurian in the Pucara
395 Basin (Schaltegger et al., 2008; Guex et al., 2012). The duration of the Sinemurian Stage
396 was relatively poorly constrained at ~ 7.62 Myr, based on assumed constant
397 sedimentation rates and a linear decrease in $^{87}\text{Sr}/^{86}\text{Sr}$ (Weedon and Jenkyns, 1999).

398 Acknowledging recognized depositional gaps, earlier astrochronological analyses
399 of the Pliensbachian in Dorset and Yorkshire (UK) and Breggia Gorge (Switzerland),
400 suggested a minimum Pliensbachian Stage duration of 4.82 Myr (Weedon and Jenkyns,
401 1999); adjustment of these data to an assumed linear decrease in seawater $^{87}\text{Sr}/^{86}\text{Sr}$ of
402 0.000042 per Myr for the Belemnite Marl Member, lengthened this minimum duration of
403 the Pliensbachian Stage to ~ 6.67 Myr (Weedon and Jenkyns, 1999). The $^{87}\text{Sr}/^{86}\text{Sr}$ -based
404 estimate of a ~ 3.96 Myr long, combined *margaritatus* and *spinatum* zone duration
405 (McArthur et al., 2000), would suggest a much longer duration for the complete
406 Pliensbachian Stage.

407 Absolute age constraints for the base Toarcian are relatively weak. U-Pb
408 radiometric dating of Lower Jurassic volcanic ashes from the North American Cordillera,
409 integrated with ammonite biochronology, gives ages of $185.7 +0.5/-0.6$ Ma for the base
410 of the *kunae* zone (which slightly predates the base of the European *margaritatus*
411 ammonite zone), $184.1 +1.2/-1.6$ Ma for the base of the *carlottense* zone (which is

412 equivalent to the European *spinatum* ammonite zone), 183.6 +1.7/−1.1 Ma for the base
413 of the *kanense* zone (which represents the Pliensbachian–Toarcian boundary and which is
414 equivalent to the combined European *tenuicostatum* and *falciferum* ammonite zones), 182.0
415 +3.3/−1.8 Ma for the base of the *planulata* zone (which is equivalent to the European
416 *bifrons* ammonite zone), and 181.4 ±1.2 Ma for the base of the *crassicosta* zone (which
417 slightly post-dates the onset of the European *variabilis* ammonite zone) (Pálffy and Smith,
418 2000). Furthermore, a Re-Os isochron age based on several combined stratigraphical
419 levels in the *falciferum* ammonite zone of the Jet Rock (Yorkshire, UK) suggests an age of
420 178 ±5 Ma for this time interval (Cohen et al., 2004). The methodological uncertainty on
421 these earlier U-Pb and Re-Os radiometric dates is, however, relatively large, and much
422 larger than one would ideally use for creating tie-points in a floating astrochronological
423 time scale.

424 A bentonite at the base of the *falciferum*-equivalent ammonite zone (*levisoni*-
425 equivalent ammonite subzone) in the Pucara Basin (Peru) was more recently
426 radiometrically (U-Pb) dated at 183.22 ± 0.25 Myr (Sell et al., 2014). The relatively scarce
427 ammonite occurrences in this section, combined with the bio- and chemostratigraphical
428 uncertainty in correlation to the European realm (Guex et al., 2012), however, do also
429 pose a problem for firmly anchoring the Early Toarcian zones to the numerical time
430 scale. For now, these data, however, provide the basis for the least uncertain age estimate
431 for this time interval, and are therefore used here to anchor the top of the Pliensbachian
432 to the numerical time scale (Figure 6).

433 The *falciferum* ammonite zone follows the lowest Toarcian *tenuicostatum* zone in
434 northwest Europe and the age-equivalent *polymorphum* zone in the Lusitanian Basin of
435 Portugal. The duration of the *polymorphum* (and *tenuicostatum*) ammonite zone was
436 astrochronologically constrained to 600–900 Kyr at Peniche in the Lusitanian Basin
437 (Suan et al., 2008; Huang and Hesselbo, 2014; Ruebsam et al., 2014, 2015), to ~550 Kyr
438 in the Lorraine Sub-Basin, France, and to a significantly shorter duration of 90–500 Kyr
439 in the Sancerre core of the Paris Basin, France (Boulila et al., 2014). The large range in
440 the Sancerre estimate primarily derived from biostratigraphical uncertainty on the exact
441 position of the lowermost Toarcian in that core. Furthermore, the Lower Toarcian
442 sedimentary record in the Lorraine Sub-Basin and especially also in the Paris Basin is
443 marked by stratigraphical condensation, possibly in response to coeval sea-level change,
444 which compromises the reliability of astrochronological constraints for this time interval,
445 based on the sedimentary successions of these two depocentres (Boulila et al., 2014;
446 Ruebsam et al., 2014, 2015). Assuming (1) the 183.22 ± 0.25 Myr radiometric age for the
447 base of the *falciferum* zone in the Pucara Basin, Peru (Sell et al., 2014), (2) a synchronous
448 age for the *tenuicostatum*–*falciferum* zonal boundary in north-western Europe, the *kanense*–
449 *planulata* zonal boundary in South America, and the *polymorphum*–*levisoni* zonal boundary
450 in the Lusitanian Basin, and (3) a ~600 ± 150 Kyr duration for the *polymorphum*
451 (*tenuicostatum*) zone, a 183.8 ± 0.4 Ma age can, tentatively, be assigned to the base of the
452 Toarcian (Figure 6).

453 The duration of the combined Toarcian *tenuicostatum* and *falciferum* zones is
454 currently much debated, with estimates ranging from ~1.9 Myr (Suan et al., 2008), to
455 ~1.4 or 2.4 Myr (Kemp et al., 2011), ~2.5 Myr (Huang and Hesselbo, 2014), ~1.54–1.71
456 Myr (Boulila et al., 2014) and >1.8 Myr (Ruebsam et al., 2014, 2015), depending primarily
457 on differences in the precession versus obliquity versus eccentricity interpretation of
458 astronomically forced steps in the Early Toarcian carbon-isotope ($\delta^{13}\text{C}$) and other
459 geochemical proxy records. Seawater $^{87}\text{Sr}/^{86}\text{Sr}$ -based estimates for this time interval
460 suggested a duration of ~1.694 Myr (McArthur et al., 2000), but this figure is problematic
461 because of large-scale tectono-climatic events over this time interval that may have

462 significantly varied Sr fluxes from both mantle and continental sources, and because of a
463 distinctly European epicontinental data bias.

464 The radiometrically constrained age of 199.43 ± 0.10 Ma for the base-Sinemurian
465 and the 183.8 ± 0.4 Ma age assigned here for the base Toarcian, suggest a ~ 15.6 Myr
466 duration for the combined Sinemurian and Pliensbachian Stages (Schaltegger, 2008;
467 Schoene, et al., 2010; Guex et al., 2012). In conjunction with the ~ 8.7 Myr duration of
468 the Pliensbachian Stage estimated here, we suggest that the Sinemurian Stage was ~ 700
469 Kyr shorter than previously estimated and had a duration of 6.9 ± 0.4 Myr, with a 192.5
470 ± 0.4 Ma age for the base-Pliensbachian (the ± 0.4 Ma uncertainty derives from the
471 combined radiometric and astrochronological uncertainty on the age of Early Toarcian
472 ash-beds in Peru and the duration of the Early Toarcian *tenuicostatum* zone, respectively)
473 (Figure 6; Table 1).

474 An astronomically calibrated absolute time scale has been constructed
475 successfully for the Neogene and part of the Paleogene (Hilgen et al., 2014).
476 Astronomical solutions for the geological past, however, become increasingly uncertain,
477 especially before ~ 50 Ma, due to multiple secular resonances in the inner solar system,
478 and in particular with respect to the θ argument ($\theta = (s_4 - s_3) - 2(g_4 - g_3)$, where g_3 and g_4
479 are related to precession of the perihelion and s_3 and s_4 are related to precession of the
480 node of Earth and Mars) (Laskar et al., 2004, 2011). The 405 Kyr eccentricity cycle,
481 related to the $(g_2 - g_5)$ argument, which reflects the motions of the orbital perihelia of
482 (gravitational pull between) Jupiter and Venus, however, remained relatively stable over
483 the past 250 Myr (Laskar et al., 2004). Different solutions for the 405 Kyr periodicity
484 show a maximum deviation of 2π over 250 Myr, corresponding to a maximum error of
485 <350 Kyr at 200 Ma (Laskar et al., 2004, 2011). The 405 Kyr eccentricity solution,
486 combined with precise radiometric anchor points, can therefore be used as a target curve
487 for the astronomical tuning of floating astronomical time scales, potentially even back
488 into the Mesozoic.

489 Precise radiometric and astrochronological age constraints for the base of the
490 Hettangian and the base of the Sinemurian potentially allow the Hettangian floating
491 astronomical time scales to be accurately anchored to the stable 405 Kyr eccentricity
492 solution (La2010d) of Laskar et al. (2011) (Figure 6). However, given the radiometric and
493 astrochronological uncertainties for the age of the base-Toarcian, and with that the age
494 of the base-Pliensbachian, we are presently unable to uniquely anchor the Pliensbachian
495 floating astronomical time scale obtained here to the absolute (numerical) time scale and
496 405 Kyr astronomical solution of Laskar et al. (2011). We therefore propose 3 different
497 models, Options A, B and C (Figure 6). Option-A represents the solution with the
498 youngest base Jurassic and oldest base Toarcian, Option-B represents the solution with
499 the oldest base Jurassic and youngest base Toarcian, and Option-C represents the
500 intermediate case (Figure 6). Importantly, different solutions for the 405 Kyr periodicity
501 show a maximum deviation of <350 Kyr in the Early Jurassic (Laskar et al., 2004), which
502 adds additional uncertainty to this tuning. Consequently, it is currently not possible to
503 assign with confidence particular observed peaks in the proxy records to either the
504 maxima or minima of the 405 Kyr eccentricity cycle.

505 Astronomically forced changes in bed thickness in the Early Jurassic pelagic chert
506 sequences from the Panthalassic Ocean (Inuyama, Japan) show also dominant precession
507 and short and long eccentricity periodicities (Ikeda and Hori, 2014; Ikeda and Tada,
508 2014). The end-Triassic mass extinction event and the Pliensbachian–Toarcian boundary
509 are well constrained in these successions, with radiolarian biostratigraphy allowing
510 biostratigraphical correlation with North American and European ammonite zones
511 (Hori, 1990, 1992, 1997). Interestingly, the number of recognised ~ 405 Kyr eccentricity
512 cycles across the Hettangian to Pliensbachian stages in the Inuyama chert sequence

513 directly match the number of 405 kyr eccentricity cycles suggested here for this time-
514 period (Option C, Figure 6). Although the Hettangian–Sinemurian and Sinemurian–
515 Pliensbachian boundary are biostratigraphically not very well constrained in the Inuyama
516 chert sequences, Early Jurassic high-resolution astrochronological correlation may be
517 possible between the pelagic and the continental margin realms of the Panthalassa Ocean
518 and the western Tethys, respectively.

519

520 [5.6] RATE AND DURATION OF PLIENSBACHIAN CLIMATIC AND GLOBAL 521 CARBON-CYCLE CHANGE

522 The Early Jurassic was marked by large perturbations in global geochemical cycles,
523 palaeoclimate and the palaeoenvironment, especially at the Triassic–Jurassic transition
524 and in the Early Toarcian (Hesselbo et al., 2002; Jenkyns, 2003, 2010; Korte et al., 2009;
525 Korte and Hesselbo, 2011; Ruhl et al., 2011; Suan et al., 2011; Ullmann et al., 2014;
526 Brazier et al., 2015; Krencker et al., 2015; Al-Suwaidi et al., 2016; and many others).

527 Recent studies show that the Pliensbachian Stage was also marked by major
528 perturbations in the global carbon cycle and possibly (global) climate. The Early
529 Pliensbachian *jamesoni* zone is marked by a negative shift in $\delta^{13}\text{C}$ (of 2–4‰) in marine
530 calcite and organic matter (Jenkyns et al., 2002; van de Schootbrugge et al., 2005;
531 Woodfine et al., 2008; Korte and Hesselbo, 2011; Armendariz et al., 2012; Franceschi et
532 al., 2014; Korte et al., 2015). This shift is also seen in the $\delta^{13}\text{C}$ of wood, reflecting global
533 atmospheric change and a rearrangement of the global exogenic carbon cycle, possibly by
534 the release of isotopically depleted carbon into the ocean-atmosphere system (Korte and
535 Hesselbo, 2011). The Late Pliensbachian *margaritatus* zone (*subnodosus* and *gibbosus*
536 subzones) is further marked by a distinct positive shift in $\delta^{13}\text{C}$ of marine and terrestrial
537 organic matter, marine calcite and wood (Jenkyns and Clayton, 1986; van de
538 Schootbrugge et al., 2005; Suan et al., 2010; Korte and Hesselbo, 2011; Silva et al., 2011),
539 possibly linked to enhanced carbon burial under favourable marine redox conditions
540 (Hesselbo and Jenkyns, 1995; Suan et al., 2010; Korte and Hesselbo, 2011; Silva et al.,
541 2011; Silva and Duarte, 2015). Possible changes in Pliensbachian atmospheric $p\text{CO}_2$,
542 based on carbon-isotope and leaf stomatal index data, may have affected regional and/or
543 global temperatures (Suan et al., 2008, 2010; Korte and Hesselbo, 2011; Armendariz et
544 al., 2013; Steinthorsdottir and Vajda, 2013; Silva and Duarte, 2015).

545 The tuned astrochronological time scale for the Pliensbachian presented here,
546 suggests that the Early Pliensbachian negative CIE had a duration of ~ 2 Myr, possibly
547 linked to a recurrent phase of CAMP magmatism (see also section 5.7; Figures 7, 8). The
548 Late Pliensbachian (upper *margaritatus* zone) $\delta^{13}\text{C}$ positive excursion coincided with
549 significant sea level fluctuations, possibly in synchrony with decreasing shallow-marine
550 benthic temperatures (Hesselbo et al., 2008; Korte and Hesselbo, 2011). The Late
551 Pliensbachian (upper *margaritatus* zone) positive carbon-isotope excursion has an
552 estimated duration of ~ 0.6 Myr (Figure 7).

553

554 [5.7] CAMP VOLCANISM AND THE EARLY JURASSIC STEPPED $^{87}\text{Sr}/^{86}\text{Sr}$ 555 RECORD

556 Seawater $^{87}\text{Sr}/^{86}\text{Sr}$ ratios and strontium fluxes to the oceans are controlled by
557 hydrothermal circulation at mid-ocean ridges and other types of basalt-seawater
558 interaction, the continental weathering of silicates, and the dissolution of carbonates,
559 while the fluxes out of the ocean are primarily regulated by carbonate burial (Burke et al.,
560 1982; Elderfield, 1986; Jones et al. 1994a, b; Steuber and Veizer, 2002; Allègre et al.,
561 2010; Krabbenhöft et al., 2010; Ullmann et al., 2013). Changes in seawater $^{87}\text{Sr}/^{86}\text{Sr}$ ratios
562 can therefore be explained by the change in the relative importance of continental
563 weathering, or a change in the Sr-isotopic composition of the weathering flux, and

564 hydrothermal inputs of Sr into the oceans. The global unradiogenic strontium flux from
565 hydrothermal venting and weathering of fresh ocean-crust along mid-ocean ridges and
566 around island arcs, is probably relatively stable over shorter time scales, but may have
567 varied on tectonic time scales, with changes in the rate of ocean-crust formation along
568 mid-ocean ridge systems and changes in the global extent of spreading ridges and ocean
569 island arcs (Allègre et al., 2010; Van der Meer et al., 2014). The global unradiogenic Sr-
570 flux may also have varied on long (>Myr) Milankovitch periodicities, possibly in
571 response to eustatic sea-level change and changing mid-ocean ridge spreading rates
572 (Cohen and Coe, 2007; Crowley et al., 2015).

573 In the Early Jurassic, seawater $^{87}\text{Sr}/^{86}\text{Sr}$ ratios show an overall decrease over ~20
574 Myr towards unradiogenic values, from ~0.70775 to ~0.70705 (Jones et al., 1994a;
575 Cohen and Coe, 2007). Proto-Atlantic rifting at this time initiated on the continents, but
576 continued throughout the Jurassic as mid-ocean ridge activity. Increased mid-ocean ridge
577 spreading rates and/or the increased global extent of mid-ocean spreading ridges,
578 combined with the possible increased formation of island arcs, may have provided an
579 enhanced unradiogenic strontium flux to the global oceans (Van der Meer et al., 2014),
580 leading to the observed steady decrease in Early Jurassic seawater $^{87}\text{Sr}/^{86}\text{Sr}$ up to the
581 Pliensbachian–Toarcian boundary (Jones et al., 1994a, b; Jenkyns et al., 2002). A decline
582 in seawater $^{87}\text{Sr}/^{86}\text{Sr}$ may alternatively be explained by a decrease in the overall
583 continental weathering flux. However, in the absence of a major orogeny in the Early and
584 Middle Jurassic, the $^{87}\text{Sr}/^{86}\text{Sr}$ ratio of the global weathering flux probably remained
585 relatively stable (Jones et al., 1994b). The changing style of biomineralization shown by
586 the evolutionary adoption of calcite in Jurassic calcifying organisms, and increasing
587 pelagic calcite production, probably did not play a major role in the observed change in
588 seawater chemistry because seawater Sr/Ca ratios changed in parallel with Sr-isotope
589 ratios, indicating a likely common weathering and/or tectonic origin for both (Ullmann
590 et al., 2013).

591 The base Jurassic Hettangian Stage, however, contrasts in being marked by a ~2
592 Myr plateau, with relatively stable $^{87}\text{Sr}/^{86}\text{Sr}$ ratios of ~0.70775 (Cohen and Coe, 2007),
593 suggesting the balancing of the unradiogenic Sr flux from basalt-seawater interaction, by
594 supply of radiogenic Sr from the weathering of old continental crust. This period was
595 also marked by major flood-basalt emplacement, with the onset of CAMP volcanism in
596 the latest Triassic, coeval with the end-Triassic mass extinction, at ~201.4 Ma. Its onset
597 preceded the Triassic–Jurassic boundary, defined by the first occurrence of the Jurassic
598 ammonite species *Psiloceras spelae (tirolicum)* (and *Psiloceras spelea (spelae)*), by 100–200 Kyr
599 (Marzoli et al., 1999; Hesselbo et al., 2002; Deenen et al., 2010, 2011; Ruhl et al., 2010;
600 Schoene et al., 2010; Whiteside et al., 2010; Ruhl and Kürschner, 2011; Blackburn et al.,
601 2013; von Hillebrandt et al., 2013; Dal Corso et al., 2014; Hüsing et al., 2014).
602 Astrochronological and radiometric dating constrain emplacement of the major CAMP
603 flood-basalt pulses in the eastern North American Newark, Culpeper, Hartford and
604 Deerfield basins, the Canadian Fundy Basin, the Algarve in Portugal, the Moroccan
605 Argana Basin and the Moroccan High Atlas Mountains, within a relatively short period
606 of time, possibly within 1 Myr after its onset (Olsen et al., 2003; Deenen et al., 2010,
607 2011; Marzoli et al., 2011; Fernandes et al., 2014). The chemical weathering of juvenile
608 basaltic rocks from CAMP is, however, unlikely to have been directly responsible for
609 stabilizing the Hettangian seawater $^{87}\text{Sr}/^{86}\text{Sr}$ signal, because Sr-isotope values of fresh
610 Large Igneous Province basalts (with values of 0.704–0.706), are much less radiogenic
611 than ambient Early Jurassic seawater (Cohen and Coe, 2007).

612 The release of volcanogenic CO₂ and biogenic and thermogenic methane from
613 sea-floor clathrates and subsurface organic-rich facies following CAMP flood-basalt
614 emplacement and dyke and sill intrusions (Hesselbo et al., 2002; Korte et al. 2009; Ruhl

615 et al., 2011; Schaller et al., 2011), combined with enhanced greenhouse-gas-induced
616 elevated hydrological cycling (Ruhl et al., 2011; Bonis and Kürschner, 2012), may have
617 enhanced the global weathering of crustal silicates, carbonates and evaporates, and the
618 consequent flux of more radiogenic Sr to the global oceans (Jones and Jenkyns, 2001;
619 Cohen and Coe, 2007).

620 CAMP-attributed flood-basalt emplacement and dyke and sill intrusions may,
621 however, have continued for millions of years into the Early Jurassic, with a late phase of
622 CAMP magmatism dated as of Early–Middle Pliensbachian age by $^{40}\text{Ar}/^{39}\text{Ar}$ (Baksi and
623 Archibald, 1997; Deckart et al., 1997; Marzoli et al., 1999; Hames et al., 2000; Knight et
624 al., 2004; Marzoli et al., 2004; Beutel et al., 2005; Verati et al., 2007; Nomade et al., 2007;
625 Jourdan et al., 2009; Marzoli et al., 2011).

626 Sinemurian and Pliensbachian seawater $^{87}\text{Sr}/^{86}\text{Sr}$ ratios are often considered to
627 show a relatively constant decline towards the Early Toarcian minimum (with values
628 down to ~ 0.70705), at which point relatively enhanced continental silicate weathering in
629 response to Early Toarcian Karoo–Ferrar volcanism induced a rapid reversal of this trend
630 to renewed relatively elevated seawater $^{87}\text{Sr}/^{86}\text{Sr}$ values (Cohen and Coe, 2007). However,
631 this supposed constant rate of decline in seawater $^{87}\text{Sr}/^{86}\text{Sr}$ may be an artefact of the
632 assumption of equal duration ammonite (sub-)zones. Conversion of the Pliensbachian
633 seawater $^{87}\text{Sr}/^{86}\text{Sr}$ record of Jones et al. (1994) and Jenkyns et al. (2002) to the
634 Pliensbachian astrochronological time scale proposed here shows 4 distinct phases of
635 enhanced decline in seawater $^{87}\text{Sr}/^{86}\text{Sr}$ superimposed on the Early Jurassic long-term fall
636 in values, with a potential periodicity of ~ 2.4 Myr (Figure 8). The veracity of the
637 observed changes in this trend relies on the accuracy of the positioning of the base of
638 individual (sub)zones in both the outcrops and especially the Mochras core, and their
639 precision as time markers. Although ammonite stratigraphy in cores might generally be
640 less precise compared to that in outcrops, where fossil occurrences can be traced
641 laterally, along geographically extensive bedding-planes, the precision of the assigned
642 bases of (sub)zones in the Mochras core is relatively good (Table 1; Supplementary
643 Figure 7) and was further refined by the identification and correlation of recognized
644 foraminiferal zones (Copestake and Johnson, 2013).

645 Phases of enhanced decline in seawater $^{87}\text{Sr}/^{86}\text{Sr}$ may reflect periodic, long-term
646 ($> \text{Myr}$) Milankovitch-forced, decreases in global continental weathering rates, with a
647 diminished flux of radiogenic Sr. Interestingly, the onset of the Pliensbachian Stage is
648 also marked by a plateau in seawater $^{87}\text{Sr}/^{86}\text{Sr}$ ratios, with stable values for ~ 2 Myr,
649 closely resembling the pattern in the base Jurassic Hettangian Stage during the major
650 phase of CAMP emplacement (Figure 8). This plateau in $^{87}\text{Sr}/^{86}\text{Sr}$ temporally coincides
651 with a late phase of CAMP magmatism, with surface flood-basalt and subsurface sill
652 emplacement in the eastern USA, Brazil and Guinea (Figure 8; Deckart et al., 1997;
653 Marzoli et al., 1999; Nomade et al., 2007). The onset and duration of this plateau in
654 $^{87}\text{Sr}/^{86}\text{Sr}$ also directly coincides with the earliest Pliensbachian (*jamesoni* zone) negative
655 CIE, similar in magnitude ($\sim 2\text{--}4\text{‰}$) and duration to the earliest Jurassic (Hettangian)
656 long-term ‘main’ negative CIE (Figure 8; Hesselbo et al., 2002; Korte et al., 2009; Ruhl et
657 al., 2010; Bartolini et al. 2012). The observed Early Pliensbachian plateau in $^{87}\text{Sr}/^{86}\text{Sr}$
658 ratios may, therefore, reflect a second Early Jurassic phase of CAMP-induced climatic
659 and carbon-cycle perturbation that, as inferred for the Hettangian, also led to increased
660 global weathering and an enhanced radiogenic Sr flux from the continents to the oceans.
661 The inference of the Early Pliensbachian plateau in $^{87}\text{Sr}/^{86}\text{Sr}$ ratios depends on (1) the
662 correct biostratigraphical correlation between the $^{87}\text{Sr}/^{86}\text{Sr}$ record, as measured in
663 outcrops, and the Mochras core-based Early Pliensbachian astrochronology and (2) the
664 correctness of the interpreted unequal duration of Pliensbachian zones, specifically the
665 Early Pliensbachian (*jamesoni*) (sub)zones. If all the above is correct, then one may

666 conclude that subsequent phases of CAMP volcanism led to elevated atmospheric $p\text{CO}_2$
667 and increased global continental (silicate) weathering rates that balanced the dominant
668 long-term unradiogenic marine hydrothermal/basalt weathering Sr flux and resulted in
669 the observed (Hettangian and Early Pliensbachian) ~ 2 Myr plateaus in the Early Jurassic
670 $^{87}\text{Sr}/^{86}\text{Sr}$ record.

671

672 [6] CONCLUSIONS

673 Periodic alternations in lithology and geochemical palaeoenvironmental proxies through
674 the expanded and biostratigraphically complete Pliensbachian of the Mochras core
675 (Llanbedr/ Mochras Farm borehole, Wales, UK) reflect Milankovitch forcing,
676 predominantly at precession and short- and long-eccentricity periodicities. The duration
677 of Pliensbachian ammonite zones is cyclostratigraphically constrained at ~ 2.7 Myr
678 (*jamesoni*), ~ 1.8 Myr (*ibex*), ~ 0.4 Myr (*davoei*), ~ 2.4 Myr (*margaritatus*) and ~ 1.4 Myr
679 (*spinatum*), with a combined duration of ~ 8.7 Myr for the complete Pliensbachian Stage.
680 These figures, combined with radiometric and astrochronological constraints on the age
681 of the base of the Toarcian, suggest a Sinemurian–Pliensbachian boundary age of 192.5
682 ± 0.4 Ma.

683 Calibration of the floating astronomical time scale for the Pliensbachian to the
684 405 Kyr eccentricity solution (La2010d) gives absolute ages for the Pliensbachian
685 ammonite biozone boundaries and the base Pliensbachian (*jamesoni* zone) global exogenic
686 carbon cycle perturbation. The negative excursion in $\delta^{13}\text{C}$ in the base Pliensbachian has a
687 2–4‰ amplitude and an astrochronologically defined duration of ~ 2 Myr. The Late
688 Pliensbachian (upper *margaritatus* zone) global positive excursion in $\delta^{13}\text{C}$, which coincides
689 with a seawater cool phase in the European realm as revealed by $\delta^{18}\text{O}$ from macrofossil
690 calcite, has a duration of ~ 0.6 Myr.

691 Calibration of the Pliensbachian $^{87}\text{Sr}/^{86}\text{Sr}$ record to the obtained
692 astrochronological age model suggests modulation with a ~ 2.4 Myr periodicity of the
693 Pliensbachian long-term decreasing trend to less radiogenic values. The Pliensbachian
694 $^{87}\text{Sr}/^{86}\text{Sr}$ record also shows a stable plateau in the Early Pliensbachian *jamesoni* zone,
695 coinciding with the observed $\delta^{13}\text{C}$ negative shift of 2–4‰, and possibly reflecting
696 elevated continental weathering, with a relatively increased flux of radiogenic $^{87}\text{Sr}/^{86}\text{Sr}$ to
697 the global oceans, in response to a late phase of enhanced global continental (silicate)
698 weathering induced by CAMP volcanism.

699

700 ACKNOWLEDGEMENTS

701 We acknowledge funding for this study from Shell International Exploration &
702 Production B.V., the International Continental Drilling Programme, and the Natural
703 Environment Research Council (NE/G01700X/1). CVU acknowledges funding from
704 Leopoldina, German National Academy of Sciences (grant no. LPDS 2014-08). We
705 thank the British Geological Survey (BGS) for enabling access to the Mochras core and
706 Charles J.B. Gowing (BGS) for supplying hand-held XRF equipment and assistance with
707 analyses. We also thank Steve Wyatt (Oxford) and Mabs Gilmour (Open University) for
708 help with Rock-Eval and $\delta^{13}\text{C}$ analyses. We are further grateful for the constructive
709 reviews by Wolfgang Ruebsam, Blair Schoene and one anonymous reviewer, and the
710 editorial guidance by Martin Frank. JBR publishes with the approval of the Executive
711 Director, British Geological Survey (NERC).

712

713 FIGURE CAPTIONS

714

715 FIGURE 1 Early Jurassic palaeogeography showing the Mochras (Cardigan Bay
716 Basin) and Staithes (Cleveland Basin) localities (red stars) at the northwestern extremity

717 of the Tethys Ocean. The figure is modified after Dera et al. (2011) and Korte et al.
718 (2015).

719

720 FIGURE 2 The relative thickness of the Lower Jurassic stages in the Mochras core
721 and outcrops and boreholes in the UK, France and Portugal (Ivimey-Cook, 1971; Cope
722 et al., 1980; Whittaker and Green, 1983; Lorenz and Gely, 1994; Ainsworth and Riley,
723 2010; Brigaud et al., 2014; Mattioli et al., 2013; and references therein). The ‘T’, ‘HS’ and
724 ‘PL’ numbers refer to the stratigraphical columns in Cope et al. (1980).

725

726 FIGURE 3 Early Pliensbachian (*jamesoni* zone) lithology and XRF-derived
727 geochemical data (calcium, titanium, iron, rubidium) showing sub-metre scale
728 fluctuations. Calcium concentrations are superimposed on stacked core photographs
729 showing a clear association with lithology/rock-colour. Four to five carbonate beds are
730 grouped into bundles (E^{-1}) and super-bundles (E^{-2}), hypothetically representing short
731 (~ 100 Kyr) and long (~ 405 Kyr) eccentricity. High values for Ti, Fe and Rb correlate
732 closely with periodically low concentrations of Ca, suggesting carbonate dilution of other
733 sedimentary components.

734

735 FIGURE 4 XRF-derived calcium and titanium record spanning the entire
736 Pliensbachian Stage (from the Late Sinemurian *raricostatum* zone into the Early Toarcian
737 *tenuicostatum* zone). Mochras core biostratigraphy following Ivimey-Cook (1971), Page
738 (2003), and Copestake and Johnson (2013). The palaeomagnetic field directions from
739 numerous outcrop studies are correlated to the Mochras core biostratigraphical record
740 following the Geological Time Scale (GTS) 2012 (Gradstein et al., 2012). Ca content,
741 superimposed on the stacked core photograph record, shows short-, intermediate- and
742 long-periodicity fluctuations, with (A) the complete core, (B) part of the Late Sinemurian
743 *raricostatum* and complete Early Pliensbachian *jamesoni* ammonite zones, (C) the
744 Pliensbachian *ibex* and *davoei* ammonite zones and (D) the Upper Pliensbachian
745 *margaritatus* and *spinatum* ammonite zones. The short- and intermediate-periodicity band-
746 pass filters reflect dominant spectral peaks in the depth-domain (Supplementary Figure 2;
747 see also section 5.3), suggesting a combined duration of ~ 8.7 Myr for the complete
748 Pliensbachian Stage (see Supplementary Figure 4). Grey arrows show intervals with
749 possibly dominant obliquity forcing.

750

751 FIGURE 5 Multi-taper (MTM; 3π) spectral and wavelet analyses of the XRF
752 elemental (Fe) time series obtained using the Astrochron toolkit (R (3.1.2) Package for
753 astrochronology, version 0.3.1; Meyers, 2014), with robust red noise models (Mann and
754 Lees, 1996). The elemental Fe record was first re-sampled to uniform sample spacing
755 using linear interpolation. Initial spectral analysis was performed with AnalySeries on a
756 detrended data-series (with low band-pass filtering to remove >150 m periodicities).
757 Dominant spectral components (Supplementary Figures 2, 3) were filtered from the data
758 series and compared to the visually defined precession and short- and long-eccentricity
759 periodicities (Figure 4). The elemental Fe record in the depth domain was subsequently
760 converted to the time domain following the observed 405 Kyr eccentricity cycles. The
761 multi-taper (MTM; 3π) spectral and wavelet analyses of the obtained elemental (Fe) time
762 series show dominant and significant peaks at precession (~ 21 and ~ 26 Kyr), obliquity
763 (~ 41 Kyr), short-period eccentricity (~ 100 and ~ 134 Kyr), long-period eccentricity
764 (~ 405 Kyr) and also long-term periodicity (~ 640 and 2500 Kyr).

765

766 FIGURE 6 Calibration of the obtained Pliensbachian 405-Kyr eccentricity series to
767 the astronomical solution (La2010d) of Laskar et al. (2011) allows for 3 different options

768 (A, B and C) due to the ~250 Kyr uncertainty in U-Pb radiometric dating of the base
769 *falciferum* zone in the Pucara Basin in Peru and the ~200 Kyr uncertainty in the
770 astrochronologically estimated duration of the base Toarcian *polymorphum* (*tenuicostatum*)
771 zone in the Lusitanian Basin, Portugal (see also section 7.2). Radiometric and
772 astrochronological constraints on the age of the base-Hettangian (Triassic–Jurassic) and
773 base-Sinemurian Stage boundaries and the duration of the Hettangian Stage and the
774 *polymorphum* zone are from Kent and Olsen (2008), Schaltegger et al. (2008), Suan et al.
775 (2008), Ruhl et al. (2010), Schoene et al. (2010), Guex et al. (2012), Blackburn et al.
776 (2013), Huang and Hesselbo (2014), Hüsing et al. (2014) and Sell et al. (2014). Orange
777 bars present the reported radiometric uncertainty. The Hettangian palaeomagnetic record
778 is from Kent and Olsen (2008) and Hüsing et al. (2014). The Pliensbachian
779 palaeomagnetic record is from the Geological Time Scale (GTS) 2012 (Gradstein et al.,
780 2012).

781

782 FIGURE 7 The Pliensbachian $\delta^{13}\text{C}$ record of marine calcite and wood from UK
783 outcrops (Jenkyns et al., 2002; Korte and Hesselbo, 2011) and $\delta^{13}\text{C}$ of bulk organic
784 matter ($\delta^{13}\text{C}_{\text{TOC}}$) from Staithes (this study; Yorkshire, UK (locality described in Korte and
785 Hesselbo, 2011)), calibrated to the Pliensbachian floating astronomical time scale, using
786 zone boundaries as tie-points and linear-interpolation within a zone.

787

788 FIGURE 8 The Pliensbachian seawater $^{87}\text{Sr}/^{86}\text{Sr}$ record calibrated against the newly
789 derived floating astrochronological time scale, using subzone boundaries in outcrops
790 (that yielded $^{87}\text{Sr}/^{86}\text{Sr}$ data) and the Mochras core as tie-points, and linear interpolation
791 within subzones. The time-calibrated $^{87}\text{Sr}/^{86}\text{Sr}$ record shows periodically enhanced
792 decline (grey arrows) superimposed on a long-term decrease from ~0.70745 to ~0.70710.
793 The base of the Pliensbachian is, furthermore, marked by a plateau in $^{87}\text{Sr}/^{86}\text{Sr}$ (blue
794 arrows), coinciding with a global carbon-cycle perturbation and recurrent Central
795 Atlantic Magmatic Province (CAMP) volcanism. Early Jurassic $^{87}\text{Sr}/^{86}\text{Sr}$ values are from
796 Jones et al. (1994b) and Jenkyns et al. (2002) (data were normalized to a value of the
797 NBS987 standard of 0.710250, with 24×10^{-6} added to the published data of Jones et al.
798 (1994b), which was normalized to a different standard). The Pliensbachian $\delta^{13}\text{C}$ record is
799 from Jenkyns et al. (2002) and Korte and Hesselbo (2011). Upper Triassic/Lower
800 Jurassic radiometric dating of CAMP magmatism comes from Baksi and Archibald
801 (1997), Deckart et al. (1997), Marzoli et al. (1999), Hames et al. (2000), Marzoli et al.
802 (2004), Knight et al. (2004), Beutel et al. (2005), Verati et al. (2007), Nomade et al. (2007),
803 Jourdan et al. (2009), Marzoli et al. (2011) and Blackburn et al. (2013). The dark grey area
804 in the upper graph shows the cumulative probability of CAMP magmatism through time,
805 following uncertainties on U-Pb and the recalculated $^{40}\text{Ar}/^{39}\text{Ar}$ radiometric dates of
806 individual basalt formations.

807

808 TABLE 1 Absolute age, uncertainty and duration estimates for the (base of) the
809 Early Jurassic stages (Hettangian, Sinemurian, Pliensbachian and Toarcian) and the
810 Hettangian and Pliensbachian zones. Basal-age and durations based on Kent and Olsen
811 (2008), Schaltegger et al. (2008), Suan et al. (2008), Ruhl et al. (2010), Schoene et al.
812 (2010), Guex et al. (2012), Blackburn et al. (2013), Boulila et al., 2014; Huang and
813 Hesselbo (2014), Hüsing et al. (2014), Ruebsam et al., 2014 and Sell et al. (2014).

814

815 REFERENCES

816 Allègre, C.J., Louvat, P., Gaillardet, J., Meynadier, L., Rad, S., Capmas, F., The fundamental role
817 of island arc weathering in the oceanic Sr isotope budget. Earth and Planetary Science
818 Letters 292, p. 51–56 (2010).

- 819 Al-Suwaidi, A.H., Hesselbo, S.P., Damborenea, S.E., Mancenido, M.O., Jenkyns, H.C., Riccardi,
820 A.C., Angelozzi, G.N., Baudin, F., The Toarcian Oceanic Anoxic Event (Early Jurassic) in
821 the Neuquén Basin, Argentina: A reassessment of age and carbon-isotope stratigraphy.
822 *The Journal of Geology* 124, p. 171–193 (2016).
- 823 Armendariz, M., Rosales, I., Badenas, B., Aurell, M., Garcia-Ramos, J.C., Pinuela, L., High-
824 resolution chemostratigraphic records from the Lower Pliensbachian belemnites:
825 Palaeoclimatic perturbations, organic facies and water mass exchange (Asturian basin,
826 northern Spain). *Palaeogeography, Palaeoclimatology, Palaeoecology* 333-334, p. 178–191
827 (2012).
- 828 Armendariz, M., Rosales, I., Badenas, B., Pinuela, L., Aurell, M., Garcia-Ramos, J.C., An
829 approach to estimate Lower Jurassic seawater oxygen-isotope composition using $\delta^{18}\text{O}$ and
830 Mg/Ca ratios of belemnite calcites (Early Pliensbachian, northern Spain). *Terra Nova* 25,
831 p. 439–445 (2013).
- 832 Baksi, A.K., Archibald, D.A., Mesozoic igneous activity in the Maranhao province, northern
833 Brazil: $^{40}\text{Ar}/^{39}\text{Ar}$ evidence for separate episodes of basaltic magmatism. *Earth and*
834 *Planetary Science Letters* 151, p. 139–153 (1997).
- 835 Bartolini, A., Guex, J., Spangenberg, J.E., Schoene, B., Taylor, D.G., Schaltegger, U., Atudorei,
836 V., Disentangling the Hettangian carbon isotope record: Implications for the aftermath of
837 the end-Triassic mass extinction. *Geochemistry, Geophysics, Geosystems* 13, no. 1 (2012).
- 838 Beutel, E.K., Nomade, S., Fronabarger, A.K., Renne, P.R., Pangea’s complex breakup: A new
839 rapidly changing stress field model. *Earth and Planetary Science Letters* 236, p. 471–485
840 (2005).
- 841 Blackburn, T.J., Olsen, P.E., Bowring, S.A., McLean, N.M., Kent, D.V., Puffer, J., McHone, G.,
842 Rasbury, E.T., Et-Touhami, M., Zircon U-Pb geochronology links the end-Triassic
843 extinction with the Central Atlantic Magmatic Province. *Science* 340, p. 941–945 (2013).
- 844 Bonis, N.R., Kürschner, W.M., Vegetation history, diversity patterns, and climate change across
845 the Triassic/Jurassic boundary. *Paleobiology* 38, p. 240–264 (2012).
- 846 Boulila, S., Galbrun, B., Huret, E., Hinnov, L.A., Rouget, I., Gardin, S., Huang, C., and Bartolini,
847 A., Astronomical calibration of the Toarcian Stage: implications for sequence stratigraphy
848 and duration of the Early Toarcian OAE, *Earth and Planetary Science Letters* 386, p. 98-
849 111 (2014).
- 850 Brazier, J.-M., Suan, G., Tacaíl, T., Simon, L., Martin, J.E., Mattioli, E., Balter, V., Calcium
851 isotopic evidence for dramatic increase of continental weathering during the Toarcian
852 oceanic anoxic event (Early Jurassic). *Earth and Planetary Science Letters* 411, p. 164–176
853 (2015).
- 854 Burgess, S.D., Bowring, S.A., Fleming, T.H., Elliot, D.H., High-precision geochronology links
855 the Ferrar large igneous province with Early Jurassic ocean anoxia and biotic crisis. *Earth*
856 *and Planetary Science Letters* 415, p. 90–99 (2015).
- 857 Burke, W.H., Denison, R.E., Hetherington, E.A., Koepnick, R.B., Nelson, H.F., Otto, J.B.,
858 Variation of seawater $^{87}\text{Sr}/^{86}\text{Sr}$ throughout Phanerozoic time. *Geology* 10, p. 516–519
859 (1982).
- 860 Clemence, M.-E., Bartolini, A., Gardin, S., Paris, G., Beaumont, V., Page, K.N., Early Hettangian
861 benthic-planktonic coupling at Doniford (SW England): Palaeoenvironmental implications
862 for the aftermath of the end-Triassic crisis. *Palaeogeography, Palaeoclimatology,*
863 *Palaeoecology* 295, p. 102–115 (2010).
- 864 Close, R.A., Friedman, M., Lloyd, G.T., Benson, R.B.J., Evidence for a Mid-Jurassic Adaptive
865 Radiation in Mammals. *Current Biology* 25, p. 1–6 (2015).
- 866 Cohen, A.S., Coe, A.L., Harding, S.M., Schwark, L., Osmium isotope evidence for the regulation
867 of atmospheric CO_2 by continental weathering. *Geology* 32, n. 2, p. 157–160 (2004).
- 868 Cohen, A.S., Coe, A.L., The impact of the Central Atlantic Magmatic Province on climate and on
869 the Sr- and Os-isotope evolution of seawater. *Palaeogeography, Palaeoclimatology,*
870 *Palaeoecology* 244, p. 374–390 (2007).
- 871 Copestake, P., Johnson, B., Lower Jurassic foraminifera from the Llanbedr (Mochras Farm)
872 borehole, North Wales, UK. *Monograph of the Palaeontographical Society, London* 167,
873 p. 1–403 (2014).

- 874 Crowley, J.W., Katz, R.F., Huybers, P., Langmuir, C.H., Park, S.-H., Glacial cycles drive
875 variations in the production of oceanic crust. *Science* 347, p. 1237–1240 (2015).
- 876 Dal Corso, J., Marzoli, A., Tateo, F., Jenkyns, H.C., Bertrand, H., Youbi, N., Mahmoudi, A.,
877 Font, E., Buratti, N., Cirilli, S., The dawn of CAMP volcanism and its bearing on the end-
878 Triassic carbon cycle disruption. *Journal of the Geological Society, London* 171, p. 153–
879 164 (2014).
- 880 Deckart, K., Feraud, G., Bertrand, H., Age of Jurassic continental tholeiites of French Guyana,
881 Surinam and Guinea: Implications for the initial opening of the Central Atlantic Ocean.
882 *Earth and Planetary Science Letters* 150, p. 205–220 (1997).
- 883 Deenen, M.H.L., Krijgsman, W., Ruhl, M., The quest for chron E23r at Partridge Island, Bay of
884 Fundy, Canada: CAMP emplacement postdates the end-Triassic extinction event at the
885 North American craton. *Canadian Journal of Earth Science* 48, p. 1282–1291 (2011).
- 886 Deenen, M.H.L., Ruhl, M., Bonis, N.R., Krijgsman, W., Kuerschner, W.M., Reitsma, M., van
887 Bergen, M.J., A new chronology for the end-Triassic mass extinction. *Earth and Planetary
888 Science Letters* 291, p. 113–125 (2010).
- 889 Dera, G., Neige, P., Dommergues, J.-L., Brayard, A., Ammonite paleobiogeography during the
890 Pliensbachian–Toarcian crisis (Early Jurassic) reflecting paleoclimate, eustasy, and
891 extinctions. *Global and Planetary Change* 78, p. 92–105 (2011).
- 892 Dobson M.R., Whittington, R.J., The geology of Cardigan Bay, *Proceedings of the Geologists’
893 Association* 98, p. 331–353 (1987).
- 894 Elderfield, H., Strontium isotope stratigraphy, *Palaeogeography, Palaeoclimatology,
895 Palaeoecology* 57, p. 71–90 (1986).
- 896 Fernandes, S., Font, E., Neres, M., Martins, L., Youbi, N., Madeira, J., Marzoli, A., The Central
897 Atlantic Magmatic Province (CAMP) in Portugal, high eruption rate in one short-lived
898 volcanic pulse. *Comunicacoes Geologicas* 101, p. 1449–1453 (2014).
- 899 Fleet, A.J., Clayton, C.J., Jenkyns, H.C., Parkinson, D.N., Liassic source-rock deposition in
900 Western Europe. In: Brooks, J., Glennie, K. (Eds.), *Petroleum Geology of North-west
901 Europe*, 1, Graham and Trotman, p. 59–70 (1987).
- 902 Franceschi, M., Dal Corso, J., Posenato, R., Roghi, G., Masetti, D., Jenkyns, H.C., Early
903 Pliensbachian (Early Jurassic) C-isotope perturbation and the diffusion of the Lithiotis
904 Fauna: Insights from the western Tethys. *Palaeogeography, Palaeoclimatology,
905 Palaeoecology* 410, p. 255–263 (2014).
- 906 Gomez, J.J., Comas-Rengifo, M.J., Goy, A., Palaeoclimatic oscillations in the Pliensbachian
907 (Lower Jurassic) of the Asturian Basin (Northern Spain). *Climate of the Past Discussions*
908 11, p. 4039–4076 (2015).
- 909 Gradstein, F.M., Ogg, J.G., Schmitz, M.D., Ogg, G.M., *The Geological Time Scale 2012, Volume
910 1 & 2*, Elsevier, ISBN: 978-0-44-459390-0 & 978-0-44-459434-1 (2012).
- 911 Guex, J., Bartolini, A., Spangenberg, J., Vicente, J.-C., Schaltegger, U., Ammonoid multi-
912 extinction crises during the Late Pliensbachian–Toarcian and carbon cycle instabilities.
913 *Solid Earth Discussions* 4, p. 1205–1228 (2012).
- 914 Guex, J., Schoene, B., Bartolini, A., Spangenberg, J., Schaltegger, U., O’Dogherty, L., Taylor, D.,
915 Bucher, H., Atudorei, V., Geochronological constraints on post-extinction recovery of the
916 ammonoids and carbon cycle perturbations during the Early Jurassic. *Palaeogeography,
917 Palaeoclimatology, Palaeoecology* 346-347, p. 1–11 (2012).
- 918 Hallam, A., Origin of minor limestone-shale cycles: Climatically induced or diagenetic? *Geology*
919 14, p. 609–612 (1986).
- 920 Hallam, A., Estimates of the amount and rate of sea-level change across the Rhaetian-Hettangian
921 and Pliensbachian-Toarcian boundaries (latest Triassic to Early Jurassic). *Journal of the
922 Geological Society* 154, p. 773–779 (1997).
- 923 Hames, W.E., Renne, P.R., Ruppel, C., New evidence for geological instantaneous emplacement
924 of earliest Jurassic central Atlantic Magmatic Province basalts on the North American
925 margin. *Geology* 28, p. 859–862 (2000).
- 926 Hesselbo, S.P., Bjerrum, C.J., Hinnov, L.A., MacNiocaill, C., Miller, K.G., Riding, J.B., van de
927 Schootbrugge, B., and the Mochras Revisited Science Team, Mochras borehole revisited: a
928 new global standard for Early Jurassic earth history. *Scientific Drilling* 16, p. 81–91 (2013).

- 929 Hesselbo, S.P., Jenkyns, H.C., A comparison of the Hettangian to Bajocian successions of Dorset
930 and Yorkshire. From Taylor, P.D. (Ed.): *Field Geology of the British Jurassic*. Geological
931 Society, London, p. 105–150 (1995).
- 932 Hesselbo, S.P., Jenkyns, H.C., British Lower Jurassic sequence stratigraphy. In (de Graciansky,
933 P.C., Hardenbol, J., Jacquín, T., Farley, M. & Vail, P.R. (Eds.) *Mesozoic–Cenozoic*
934 *Sequence Stratigraphy of European Basins*. Society for Sedimentary Geology (SEPM),
935 Special Publication, 60, p. 561–581 (1998).
- 936 Hesselbo, S.P., Meister, C., Grocke, D.R., A potential global stratotype for the Sinemurian-
937 Pliensbachian boundary (Lower Jurassic), Robin Hood’s Bay, UK: ammonite faunas and
938 isotope stratigraphy. *Geological Magazine* 137, p. 601–607 (2000).
- 939 Hesselbo, S.P., Robinson, S.A., Surlyk, F., Piasecki, S., Terrestrial and marine extinction at the
940 Triassic-Jurassic boundary synchronized with major carbon-cycle perturbation: A link to
941 initiation of massive volcanism? *Geology* 30, p. 251–254 (2002).
- 942 Hesselbo, S.P., Robinson, S.A., Surlyk, F., Sea-level change and facies development across
943 potential Triassic-Jurassic boundary horizons, SW Britain. *Journal of the Geological*
944 *Society*, London 161, p. 365–379 (2004).
- 945 Hesselbo, S.P., Sequence stratigraphy and inferred relative sea-level change from the onshore
946 British Jurassic. *Proceedings of the Geologists’ Association* 119, p. 19–34 (2008).
- 947 Hilgen, F.J., Hinnov, L.A., Abdul Aziz, H., Abels, H.A., Batenburg, S., Bosmans, J.H.C., de Boer,
948 B., Hüsing, S.K., Kuiper, K.F., Lourens, L.J., Rivera, T., Tüenter, E., Van de Wal, R.S.W.,
949 Wotzlaw, J.-F., Zeeden, C., Stratigraphic continuity and fragmentary sedimentation: the
950 success of cyclostratigraphy as part of integrated stratigraphy. From: Smith, D.G., Bailey,
951 R.J., Burgess, P.M., Fraser, A.J. (eds): *Strata and Time: Probing the gaps in our*
952 *understanding*. Geological Society, London, Special Publication 404, p. 157–197 (2014).
- 953 Hori, R., Lower Jurassic radiolarian zones of SW Japan. *Transactions and Proceedings of the*
954 *Palaeontological Society of Japan*, N.S. 159, p. 562–586 (1990).
- 955 Hori, R., Radiolarian biostratigraphy at the Triassic–Jurassic period boundary in bedded cherts
956 from the Inuyama area, Central Japan. *Journal of Geosciences Osaka City University* 35, p.
957 53–65 (1992).
- 958 Hori, S.R., The Toarcian radiolarian event in bedded cherts from southwestern Japan. *Marine*
959 *Micropaleontology* 30, p. 159–169 (1997).
- 960 Huang, C., Hesselbo, S.P., Pacing of the Toarcian Oceanic Anoxic Event (Early Jurassic) from
961 astronomical correlation of marine sections. *Gondwana Research* 25, p. 1348–1356 (2014).
- 962 Hüsing, S.K., Beniést, A., Van der Boon, A., Abels, H.A., Deenen, M.H.L., Ruhl, M., Krijgsman,
963 W., Astronomically-calibrated magnetostratigraphy of the Lower Jurassic marine
964 successions at St Audrie’s Bay and East Quantoxhead (Hettangian-Sinemurian; Somerset,
965 UK). *Palaeogeography, Palaeoclimatology, Palaeoecology* 403, p. 43–56 (2014).
- 966 Ikeda, M., Hori, R.S., Effects of Karoo–Ferrar volcanism and astronomical cycles on the
967 Toarcian Oceanic Anoxic Events (Early Jurassic). *Palaeogeography, Palaeoclimatology,*
968 *Palaeoecology* 410, p. 134–142 (2014).
- 969 Ikeda, M., Tada, R., A 70 million year astronomical time scale for the deep-sea bedded chert
970 sequence (Inuyama, Japan): Implications for Triassic–Jurassic geochronology. *Earth and*
971 *Planetary Science Letters* 399, p. 30–43 (2014).
- 972 Ivimey-Cook, H.C., Stratigraphical Palaeontology of the Lower Jurassic of the Llanbedr
973 (Mochras Farm) Borehole. In: Woodland, A.W. (Ed). *The Llanbedr (Mochras Farm)*
974 *Borehole*. Institute of Geological Sciences Report No. 71/18, p. 87–92 (1971).
- 975 Jenkyns, H.C., Clayton, C.J., Black shales and carbon isotopes in pelagic sediments from the
976 Tethyan Lower Jurassic. *Sedimentology* 33, p. 87–106 (1986).
- 977 Jenkyns, H.C., Evidence for rapid climate change in the Mesozoic–Palaeogene greenhouse world.
978 *Philosophical Transactions of the Royal Society London A* 361, p. 1885–1916 (2003).
- 979 Jenkyns, H.C., Geochemistry of oceanic anoxic events. *Geochemistry, Geophysics, Geosystems*
980 11, Q03004, DOI: 10.1029/2009GC002788 (2010).
- 981 Jenkyns, H.C., Jones, C.E., Grocke, D.R., Hesselbo, S.P., Parkinson, D.N., Chemostratigraphic
982 of the Jurassic System: applications, limitations and implications for palaeoceanography.
983 *Journal of the Geological Society* 159, p. 351–378 (2002).

- 984 Jenkyns, H.C., Weedon, G.P., Chemostratigraphic (CaCO_3 , TOC, $\delta^{13}\text{C}_{\text{org}}$) of Sinemurian (Lower
985 Jurassic) black shales from the Wessex Basin, Dorset and palaeoenvironmental
986 implications. *Newsletters on Stratigraphy* 46, p. 1–21 (2013).
- 987 Jones, C.E., Jenkyns, H.C., Coe, A.L., Hesselbo, S.P., Strontium isotopic variations in Jurassic
988 and Cretaceous seawater. *Geochimica et Cosmochimica Acta* 58, p. 3061–3074 (1994 a).
- 989 Jones, C.E., Jenkyns, H.C., Hesselbo, S.P., Strontium isotopes in Early Jurassic seawater.
990 *Geochimica et Cosmochimica Acta* 58, p. 1285–1301 (1994 b).
- 991 Jones, C.E., Jenkyns, H.C., Seawater strontium isotopes, oceanic anoxic events, and seafloor
992 hydrothermal activity in the Jurassic and Cretaceous. *American Journal of Science* 301, p.
993 112–149 (2001).
- 994 Jourdan, F., Marzoli, A., Bertrand, H., Cirilli, S., Tanner, L.H., Kontak, D.J., McHone, G., Renne,
995 P.R., Bellieni, G., $^{40}\text{Ar}/^{39}\text{Ar}$ age of CAMP in North America: Implications for the Triassic-
996 Jurassic boundary and the ^{40}K decay constant bias. *Lithos* 110, p. 167–180 (2009).
- 997 Kemp, D.B., Coe, A.L., Cohen, A.S., Weedon, G.P., Astronomical forcing and chronology of the
998 Early Toarcian (Early Jurassic) oceanic anoxic event in Yorkshire, UK. *Paleoceanography*
999 26, PA4210 (2011).
- 1000 Kent, D.V., Olsen, P.E., Early Jurassic magnetostratigraphy and paleolatitudes from the Hartford
1001 continental rift basin (eastern North America): Testing for polarity bias and abrupt polar
1002 wander in association with the Central Atlantic Magmatic Province. *Journal of*
1003 *Geophysical Research* 113, B06105 (2008).
- 1004 Knight, K.B., Nomade, S., Renne, P.R., Marzoli, A., Bertrand, H., Youbi, N., The Central
1005 Atlantic Magmatic Province at the Triassic-Jurassic boundary: paleomagnetic and
1006 $^{40}\text{Ar}/^{39}\text{Ar}$ evidence from Morocco for brief, episodic volcanism. *Earth and Planetary*
1007 *Science Letters* 228, p. 143–160 (2004).
- 1008 Korte, C., Hesselbo, S.P., Jenkyns, H.C., Rickaby, R.E.M., Spotl, C., Palaeoenvironmental
1009 significance of carbon- and oxygen-isotope stratigraphy of marine Triassic Jurassic
1010 boundary sections in SW Britain. *Journal of the Geological Society* 166, p. 431–445 (2009).
- 1011 Korte, C., Hesselbo, S.P., Shallow marine carbon and oxygen isotopic and elemental records
1012 indicate icehouse-greenhouse cycles during the Early Jurassic. *Paleoceanography* 26,
1013 PA4219 (2011).
- 1014 Korte, C., Hesselbo, S.P., Ullmann, C.V., Dietl, G., Ruhl, M., Schweigert, G., Thibault, T.,
1015 Jurassic climate mode governed by ocean gateway. *Nature Communications* 6, p. 10015
1016 (2015).
- 1017 Krabbenhöft, A., Eisenhauer, A., Böhm, F., Vollstaedt, H., Fietzke, J., Liebetrau, V., Augustin,
1018 N., Peucker-Ehrenbrink, B., Muller, M.N., Horn, C., Hansen, B.T., Nolte, N., Wallmann,
1019 K., Constraining the marine strontium budget with natural strontium isotope
1020 fractionations ($^{87}\text{Sr}/^{86}\text{Sr}^*$, $\delta^{88/86}\text{Sr}$) of carbonates, hydrothermal solutions and rivers.
1021 *Geochimica et Cosmochimica Acta* 74, p. 4097–4109 (2010).
- 1022 Krencker, F.-N., Bodin, S., Suan, G., Heimhofer, U., Kabiri, L., Immenhauser, A., Toarcian
1023 extreme warmth led to tropical cyclone intensification. *Earth and Planetary Science Letters*
1024 425, p. 120–130 (2015).
- 1025 Laskar, J., Fienga, A., Gastineau, M., Manche, H., La2010: a new orbital solution for the long-
1026 term motion of the Earth. *Astronomy & Astrophysics* 532, A89 (2011).
- 1027 Laskar, J., Robutel, P., Joutel, F., Gastineau, M., Correia, A.C.M., Levrard, B., A long-term
1028 numerical solution for the insolation quantities of the Earth. *Astronomy & Astrophysics*
1029 428, p. 261–285 (2004). Mann, M.E., Lees, J.M., Robust estimation of background noise
1030 and signal detection in climatic time series. *Climatic Change* 33, p. 409–445 (1996).
- 1031 Marzoli, A., Bertrand, H., Knight, K.B., Cirilli, S., Buratti, N., Verati, C., Nomade, S., Renne,
1032 P.R., Youbi, N., Martini, R., Allenbach, K., Neuwerth, R., Rapaille, C., Zaninetti, L.,
1033 Bellieni, G., Synchrony of the Central Atlantic Magmatic Province and the Triassic-Jurassic
1034 boundary climatic and biotic crisis. *Geology* 32, p. 973–976 (2004).
- 1035 Marzoli, A., Jourdan, F., Puffer, J.H., Cuppone, T., Tanner, L.H., Weems, R.E., Bertrand, H.,
1036 Cirilli, S., Bellieni, G., De Min, A., Timing and duration of the Central Atlantic Magmatic
1037 Province in the Newark and Culpeper basins, eastern U.S.A. *Lithos* 122, p. 175–188
1038 (2011).

- 1039 Marzoli, A., Renne, P.R., Piccirillo, E.M., Ernesto, M., Bellieni, G., De Min, A., Extensive 200-
1040 million-year-old continental flood basalts of the Central Atlantic Magmatic Province.
1041 *Science* 284, p. 616 (1999).
- 1042 McArthur, J.M., Donovan, D.T., Thirlwall, M.F., Fouke, B.W., Matthey, D., Strontium isotope
1043 profile of the Early Toarcian (Jurassic) oceanic anoxic event, the duration of ammonite
1044 biozones and belemnite palaeotemperatures. *Earth and Planetary Science Letters* 179, p.
1045 269–285 (2000).
- 1046 McArthur, J.M., Steuber, T., Page, K.N., Landman, N.H., Sr-isotope stratigraphy: Assigning time
1047 in the Campanian, Pliensbachian, Toarcian and Valanginian. *The Journal of Geology* 124,
1048 p. 000–000, 2016 (2016).
- 1049 McElwain, J.C., Beerling, D.J., Woodward, F.I., Fossil plants and global warming at the Triassic-
1050 Jurassic boundary. *Science* 285, p. 1386 (1999).
- 1051 Meister, C., Aberhan, M., Blau, J., Dommergues, J.-L., Feist-Burkhardt, S., Hailwood, E.A., Hart,
1052 M., Hesselbo, S.P., Hounslow, M.W., Hylton, M., Morton, N., Page, K., Price, G., the
1053 Global Boundary Stratotype Section and Point (GSSP) for the base of the Pliensbachian
1054 Stage (Lower Jurassic), Wine Haven, Yorkshire, UK. *Episodes* 20, 93-106 (2006).
- 1055 Meyers, S.R., Astrochron: An R Package for Astrochronology (Version 0.3.1). [http://cran.r-](http://cran.r-project.org/package=astrochron)
1056 [project.org/package=astrochron](http://cran.r-project.org/package=astrochron)) (2014).
- 1057 Morettini, E., Santantonio, M., Bartolini, A., Cecca, F., Baumgartner, P.O., Hunziker, J.C.,
1058 Carbon isotope stratigraphy and carbonate production during the Early-Middle Jurassic:
1059 examples from the Umbria-Marche-Sabine Apennines (central Italy). *Palaeogeography,*
1060 *Palaeoclimatology, Palaeoecology* 184, p. 251–273 (2002).
- 1061 Nomade, S., Knight, K.B., Beutel, E., Renne, P.R., Verati, C., Feraud, G., Marzoli, A., Youbi, N.,
1062 Bertrand, H., Chronology of the Central Atlantic Magmatic Province: Implications for the
1063 Central Atlantic rifting process and the Triassic–Jurassic biotic crisis. *Palaeogeography,*
1064 *Palaeoclimatology, Palaeoecology* 244, p. 326–344 (2007).
- 1065 Olsen, P.E., Stratigraphic record of the Early Mesozoic breakup of Pangea in the Laurasia-
1066 Gondwana rift system. *Annual Review of Earth and Planetary Sciences* 25, p. 337–401
1067 (1997).
- 1068 Olsen, P.E., Kent, D.V., Et-Touhami, M., Puffer, J., Cyclo-, magneto, and bio-stratigraphic
1069 constraints on the duration of the CAMP event and its relationship to the Triassic-Jurassic
1070 boundary. From: *The Central Atlantic Magmatic Province: Insights from fragments of*
1071 *Pangea. Geophysical Monograph* 136, American Geophysical Union (2003).Page, K.N.,
1072 Bello, J., Dolores Lardies, M., Melendez, G., Ramajo, J., Ziani, H., The stratigraphy of the
1073 upper Bathonian to middle Oxfordian succession of the aragonese branch of the
1074 Cordillera Iberica (Spain) and its European context. *Rivista Italiana do Paleontologia e*
1075 *Stratigrafia* 110, p. 191–200 (2004).
- 1076 Page, K.N., The Lower Jurassic of Europe; its subdivision and correlation. *Geological Survey of*
1077 *Denmark and Greenland Bulletin* 1, p. 23–59 (2003).
- 1078 Paillard, D., Labeyrie, L., Yiou, P., Macintosh program performs time-series analysis, *Eos,*
1079 *Transactions of the American Geophysical Union* 77: 379 (1996).
- 1080 Pálffy, J., Smith, P.L., Synchrony between Early Jurassic extinction, oceanic anoxic event, and the
1081 Karoo-Ferrar flood basalt volcanism. *Geology* 28, n. 8, p. 747–750 (2000).
- 1082 Percival, L.M.E., Witt, M.L.I., Mather, T.A., Hermoso, M., Jenkyns, H.C., Hesselbo, S.P., Al-
1083 Suwaidi, A.H., Storm, M.S., Xu, W., Ruhl, M., Globally enhanced mercury deposition
1084 during the end-Pliensbachian extinction and Toarcian OAE: A link to the Karoo–Ferrar
1085 Large Igneous Province. *Earth and Planetary Science Letters* 428, p. 267–280 (2015).
- 1086 Porter S.J., Selby, D., Suzuki, K., Grocke, D., opening of a trans-Pangaeian marine corridor
1087 during the Early Jurassic: Insights from osmium isotopes across the Sinemurian-
1088 Pliensbachian GSSP, Robin Hood’s Bay, UK. *Palaeogeography, Palaeoclimatology,*
1089 *Palaeoecology* 375, p. 50–58 (2013).
- 1090 Riding, J.B., Leng, M.J., Kender, S., Hesselbo, S.P., Feist-Burkhardt, S., Isotopic and
1091 palynological evidence for a new Early Jurassic environmental perturbation.
1092 *Palaeogeography, Palaeoclimatology, Palaeoecology* 374, p. 16-27 (2013).

- 1093 Ruebsam, W., Munzberger, P., Schwark, L., Chronology of the Early Toarcian environmental
1094 crisis in the Lorraine Sub-Basin (NE Paris Basin). *Earth and Planetary Science Letters* 404,
1095 p. 273–282 (2014).
- 1096 Ruebsam, W., Munzberger, P., Schwark, L., Reply to the comment by Boulila and Hinnov
1097 towards “Chronology of the Early Toarcian environmental crisis in the Lorraine Sub-Basin
1098 (NE Paris Basin). *Earth and Planetary Science Letters* 404, p. 273–282 (2014)”. *Earth and*
1099 *Planetary Science Letters* 416, 147–150 (2015).
- 1100 Ruhl, M., Bonis, N.R., Reichart, G.-J., Sinninghe Damste, J.S., Kürschner, W.M., Atmospheric
1101 carbon injection linked to End-Triassic mass extinction. *Science* 333, p. 430 (2011).
- 1102 Ruhl, M., Deenen, M.H.L., Abels, H.A., Bonis, N.R., Krijgsman, W., Kürschner, W.M.,
1103 Astronomical constraints on the duration of the Early Jurassic Hettangian Stage and
1104 recovery rates following the end-Triassic mass extinction (St Audrie’s Bay/East
1105 Quantoxhead, UK). *Earth and Planetary Science Letters* 295, p. 262–276 (2010).
- 1106 Ruhl, M., Kürschner, W.M., Multiple phases of carbon cycle disturbance from large igneous
1107 province formation at the Triassic-Jurassic transition. *Geology* 39, p. 431–434 (2011).
- 1108 Schaller, M. F., Wright, J.D., Kent, D.V., Atmospheric pCO₂ perturbations associated with the
1109 Central Atlantic Magmatic Province. *Science* 331, p. 1404 (2011).
- 1110 Schaltegger, U., Guex, J., Bartolini, A., Schoene, B., Ovtcharova, M., Precise U-Pb age
1111 constraints for end-Triassic mass extinction, its correlation to volcanism and Hettangian
1112 post-extinction recovery. *Earth and Planetary Science Letters* 267, p. 266–275 (2008).
- 1113 Schoene, B., Guex, J., Bartolini, A., Schaltegger, U., Blackburn, T.J., Correlating the end-Triassic
1114 mass extinction and flood basalt volcanism at the 100 ka level. *Geology* 38, p. 387–390
1115 (2010).
- 1116 Sell, B., Ovtcharova, M., Guex, J., Bartolini, A., Jourdan, F., Spangenberg, J.E., Vicente, J.-C.,
1117 Schaltegger, U., Evaluating the temporal link between the Karoo LIP and climatic-biologic
1118 events of the Toarcian Stage with high-precision U-Pb geochronology. *Earth and*
1119 *Planetary Science Letters* 408, p. 48–56 (2014).
- 1120 Sellwood, B.W., Regional environmental changes across a Lower Jurassic stage-boundary in
1121 Britain. *Palaeontology* 15, p. 125 (1972).
- 1122 Sellwood, B.W., The relation of trace fossils to small scale sedimentary cycles in the British Lias.
1123 From: crimes, I.P. and Harper, J.C., (eds): *Trace Fossils*. Seel House Press, Liverpool,
1124 Special Issue *Geological Journal*, p. 489–504 (1970).
- 1125 Silva, R.L., Duarte, L.V., Comas-Rengifo, M.J., Mendonca Filho, J.G., Azeredo, A.C., Update of
1126 the carbon and oxygen isotopic records of the Early–Late Pliensbachian (Early Jurassic,
1127 ~187 Ma): Insights from the organic-rich hemipelagic series of the Lusitanian Basin
1128 (Portugal). *Chemical Geology* 283, p. 177–184 (2011).
- 1129 Silva, R.L., Duarte, L.V., Organic matter production and preservation in the Lusitanian Basin
1130 (Portugal) and Pliensbachian climatic hot snaps. *Global and Planetary Change* 131, p. 24–
1131 34 (2015).
- 1132 Steinthorsdottir, M., Vajda, V., Early Jurassic (late Pliensbachian) CO₂ concentrations based on
1133 stomatal analysis of fossil conifer leaves from eastern Australia. *Gondwana Research* 27, p.
1134 932–939 (2013).
- 1135 Steuber, T., Veizer, J., Phanerozoic record of plate tectonic control of seawater chemistry and
1136 carbonate sedimentation. *Geology* 30, p. 1123–1126 (2002).
- 1137 Suan, G., Mattioli, E., Pittet, B., Lecuyer, C., Sucheras-Marx, B., Duarte, L.V., Philippe, M.,
1138 Reggiani, L., Martineau, F., Secular environmental precursors to Early Toarcian (Jurassic)
1139 extreme climate changes. *Earth and Planetary Science Letters* 290, p. 448–458 (2010).
- 1140 Suan, G., Nikitenko, B.L., Rogov, M.A., Baudin, F., Spangenberg, J.E., Knyazev, V.G., Glinskikh,
1141 L.A., Goryacheva, A.A., Adatte, T., Riding, J.B., Föllmi, K.B., Pittet, B., Mattioli, E.,
1142 Lecuyer, C., Polar record of Early Jurassic massive carbon injection. *Earth and Planetary*
1143 *Science Letters* 312, p. 102–113 (2011).
- 1144 Suan, G., Pittet, B., Bour, I., Mattioli, E., Duarte, L.V., Maillot, S., Duration of the Early Toarcian
1145 carbon isotope excursion deduced from spectral analyses: Consequence for its possible
1146 causes. *Earth and Planetary Science Letters* 267, p. 666–679 (2008).
- 1147 Tappin, D.R., Chadwick, R.A., Jackson, A.A., Wingfield, R.T.R., Smith, N.J.P., *Geology of*
1148 *Cardigan Bay and the Bristol Channel, United Kingdom Offshore Regional Report, British*

- 1149 Geological Survey, HMSO, p. 107 (1994).
- 1150 Ullmann, C.V., Hesselbo, S.P., Korte, C., Tectonic forcing of Early to Middle Jurassic seawater
1151 Sr/Ca. *Geology* 41, p. 1211–1214 (2013).
- 1152 Ullmann, C.V., Thibault, N., Ruhl, M., Hesselbo, S.P., Korte, C., Effect of a Jurassic oceanic
1153 anoxic event on belemnite ecology and evolution. *Proceedings of the National Academy
1154 of Sciences of the United States of America* 111, p. 10073–10076 (2014).
- 1155 van Buchem, F.P.S., Knox, R.W.O'B., Lower and middle Liassic depositional sequences of
1156 Yorkshire (UK). *Mesozoic and Cenozoic Sequence Stratigraphy of European Basins*,
1157 SEPM Special Publication No. 60, p. 561–581 (1998).
- 1158 van Buchem, F.S.P., Melnyk, D.H., McCave, I.N., Chemical cyclicity and correlation of Lower
1159 Lias mudstones using gamma ray logs, Yorkshire, UK. *Journal of the Geological Society*
1160 149, p. 991–1002 (1992).
- 1161 van Buchem, F.S.P., McCave, I.N., Cyclic sedimentation patterns in Lower Lias mudstones of
1162 Yorkshire (GB). *Terra Nova* 1, p. 461–467 (1989).
- 1163 van Buchem, F.S.P., McCave, I.N., Weedon, G.P., Orbitally induced small-scale cyclicity in a
1164 siliciclastic epicontinental setting (Lower Lias, Yorkshire, UK). In: Boer, P.L., Smith, D.G.
1165 (Eds.), *Orbital forcing and cyclic sequences*. International Association of Sedimentologists
1166 Special Publication 19, p. 345–366.
- 1167 Van de Schootbrugge, B., Bailey, T.R., Rosenthal, Y., Katz, M.E., Wright, J.D., Miller, K.G.,
1168 Feist-Burkhardt, S., Falkowski, P.G., Early Jurassic climate change and the radiation of
1169 organic-walled phytoplankton in the Tethys Ocean. *Paleobiology* 31, p. 73–97 (2005).
- 1170 Van der Meer, D.G., Zeebe, R.E., van Hinsbergen, D.J.J., Sluijs, A., Spakman, W., Torsvik, T.H.,
1171 Plate tectonic controls on atmospheric CO₂ levels since the Triassic. *Proceedings of the
1172 National Academy of Sciences of the United States of America* 111, p. 4380–4385 (2014).
- 1173 Verati, C., Rapaille, C., Feraud, G., Marzoli, A., Bertrand, H., Youbi, N., ⁴⁰Ar/³⁹Ar ages and
1174 duration of the central Atlantic Magmatic Province volcanism in Morocco and Portugal
1175 and its relation to the Triassic–Jurassic boundary. *Palaeogeography, Palaeoclimatology,
1176 Palaeoecology* 244, p. 308–325 (2007).
- 1177 Von Hillebrandt, A.V., Krystyn, L., Kürschner, W.M., Bonis, N.R., Ruhl, M., Richoz, S.,
1178 Schobben, M.A.N., Urlichs, M., Bown, P.R., Kment, K., McRoberts, C.A., Simms, M.,
1179 Tomasovych, A., The Global Stratotype Sections and Point (GSSP) for the base of the
1180 Jurassic System at Kuhjoch (Karwendel Mountains, Northern Calcareous Alps, Tyrol,
1181 Austria). *Episodes* 36, p. 162–198 (2013).
- 1182 Waterhouse, H.K., Regular terrestrially derived palynofacies cycles in irregular marine
1183 sedimentary cycles, Lower Lias, Dorset, UK. *Journal of the Geological Society, London*
1184 156, p. 1113–1124 (1999).
- 1185 Weedon, G.P., Hemipelagic shelf sedimentation and climatic cycles: the basal Jurassic (Blue Lias)
1186 of South Britain. *Earth and Planetary Science Letters* 76, p. 321–335 (1985/86).
- 1187 Weedon, G.P., The detection and illustration of regular sedimentary cycles using Walsh power
1188 spectra and filtering, with examples from the Lias of Switzerland. *Journal of the
1189 Geological Society, London* 146, p. 133–144 (1989).
- 1190 Weedon, G.P., Jenkyns, H.C., Coe, A.L., Hesselbo, S.P., Astronomical calibration of the Jurassic
1191 time-scale from cyclostratigraphy in British mudrock formations. *Philosophical
1192 Transactions of the Royal Society of London A* 357, p.1787–1813 (1999).
- 1193 Weedon, G.P., Jenkyns, H.C., Cyclostratigraphy and the Early Jurassic timescale: Data from the
1194 Belemnite Marls, Dorset, southern England. *Geological Society of America Bulletin* 111,
1195 p. 1823–1840 (1999). Whiteside, J.H., Olsen, P.E., Eglinton, T., Brookfield, M.E.,
1196 Sambrotto, R., N., Compound-specific carbon isotopes from Earth's largest flood basalt
1197 eruptions directly linked to the end-Triassic mass extinction. *Proceedings of the National
1198 Academy of Sciences of the United States of America* 107, p. 6721–6725 (2010).
- 1199 Woodfine, R.G., Jenkyns, H.C., Sarti, M., Baroncini, F., Violante, C., The response of two
1200 Tethyan carbonate platforms to the Early Toarcian (Jurassic) oceanic anoxic event:
1201 environmental change and differential subsidence. *Sedimentology* 55, p. 1011–1028 (2008).
- 1202 Woodland, A.W. (Ed.), *The Llanbedr (Mochras Farm) Borehole*. Institute of Geological Sciences
1203 Report No. 71/18, p. 115 (1971).

1204 Wotzlaw, J.-F., Guex, J., Bartolini, A., Gallet, Y., Krystyn, L., McRoberts, C.A., Taylor, D.,
1205 Schoene, B., Schaltegger, U., Towards accurate numerical calibration of the Late Triassic:
1206 High-precision U-Pb geochronology constraints on the duration of the Rhaetian. *Geology*
1207 42, p. 571–574 (2014).
1208
1209
1210
1211
1212
1213
1214
1215
1216
1217
1218
1219
1220
1221
1222
1223
1224
1225
1226
1227
1228
1229
1230
1231
1232
1233
1234
1235
1236
1237
1238
1239
1240
1241
1242
1243
1244
1245
1246
1247
1248
1249
1250
1251
1252
1253
1254
1255
1256
1257
1258
1259

1260
1261
1262
1263
1264
1265
1266
1267
1268
1269
1270
1271
1272
1273
1274
1275
1276
1277
1278
1279
1280
1281
1282
1283
1284
1285
1286
1287
1288
1289
1290
1291
1292
1293
1294
1295
1296
1297
1298
1299
1300
1301
1302
1303
1304
1305
1306
1307
1308
1309
1310
1311
1312
1313
1314
1315

FIGURE 1

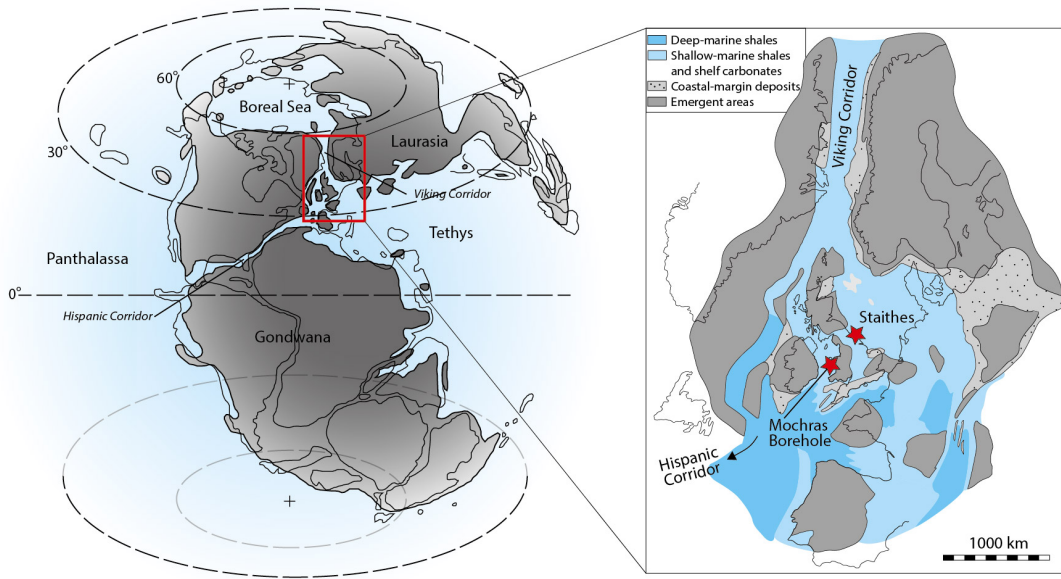
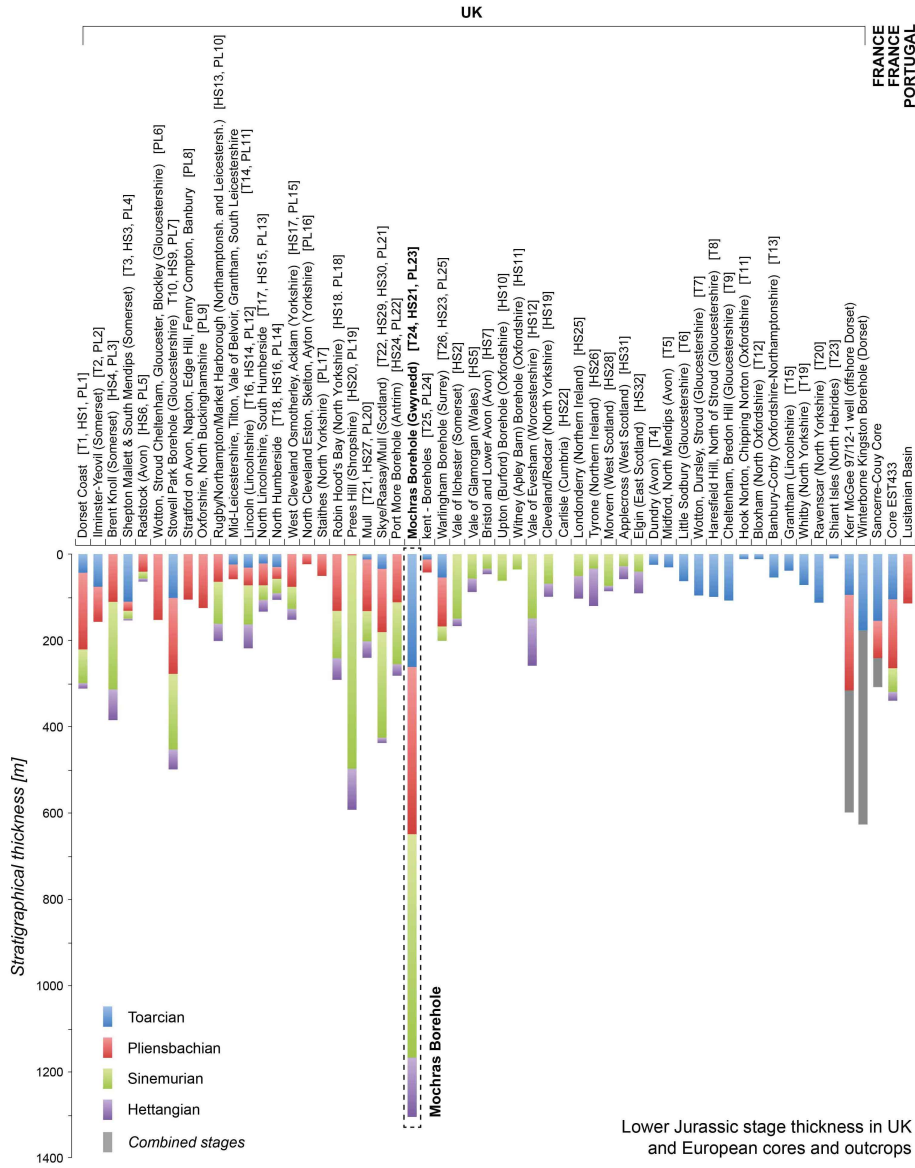


FIGURE 2



1372
 1373
 1374
 1375
 1376
 1377
 1378
 1379
 1380
 1381
 1382
 1383
 1384
 1385
 1386
 1387
 1388
 1389
 1390
 1391
 1392
 1393
 1394
 1395
 1396
 1397
 1398
 1399
 1400
 1401
 1402
 1403
 1404
 1405
 1406
 1407
 1408
 1409
 1410
 1411
 1412
 1413
 1414
 1415
 1416
 1417
 1418
 1419
 1420
 1421
 1422
 1423
 1424
 1425
 1426
 1427

FIGURE 3

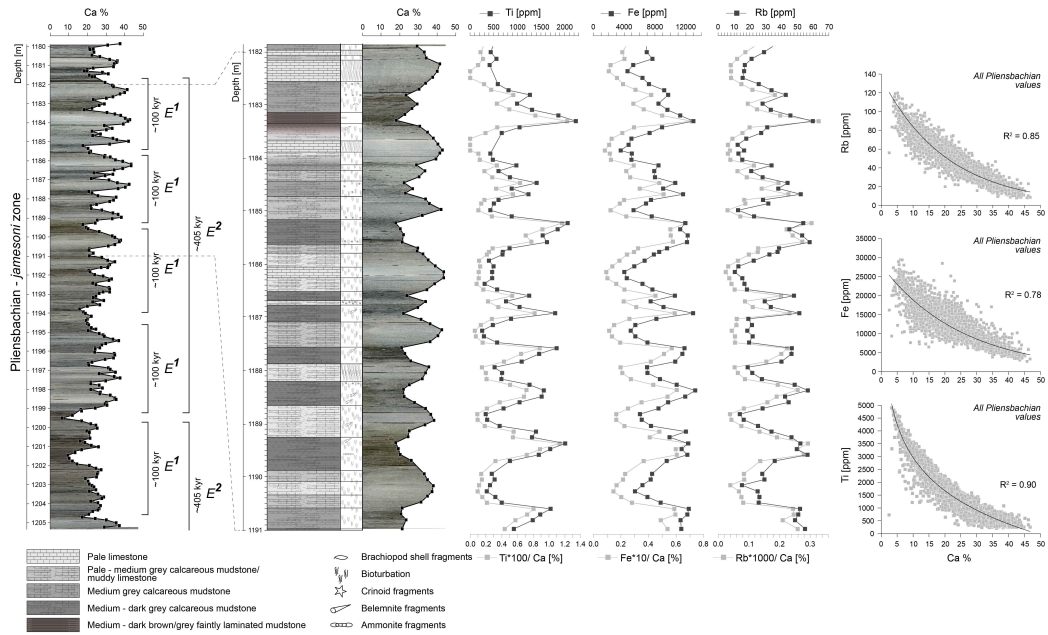
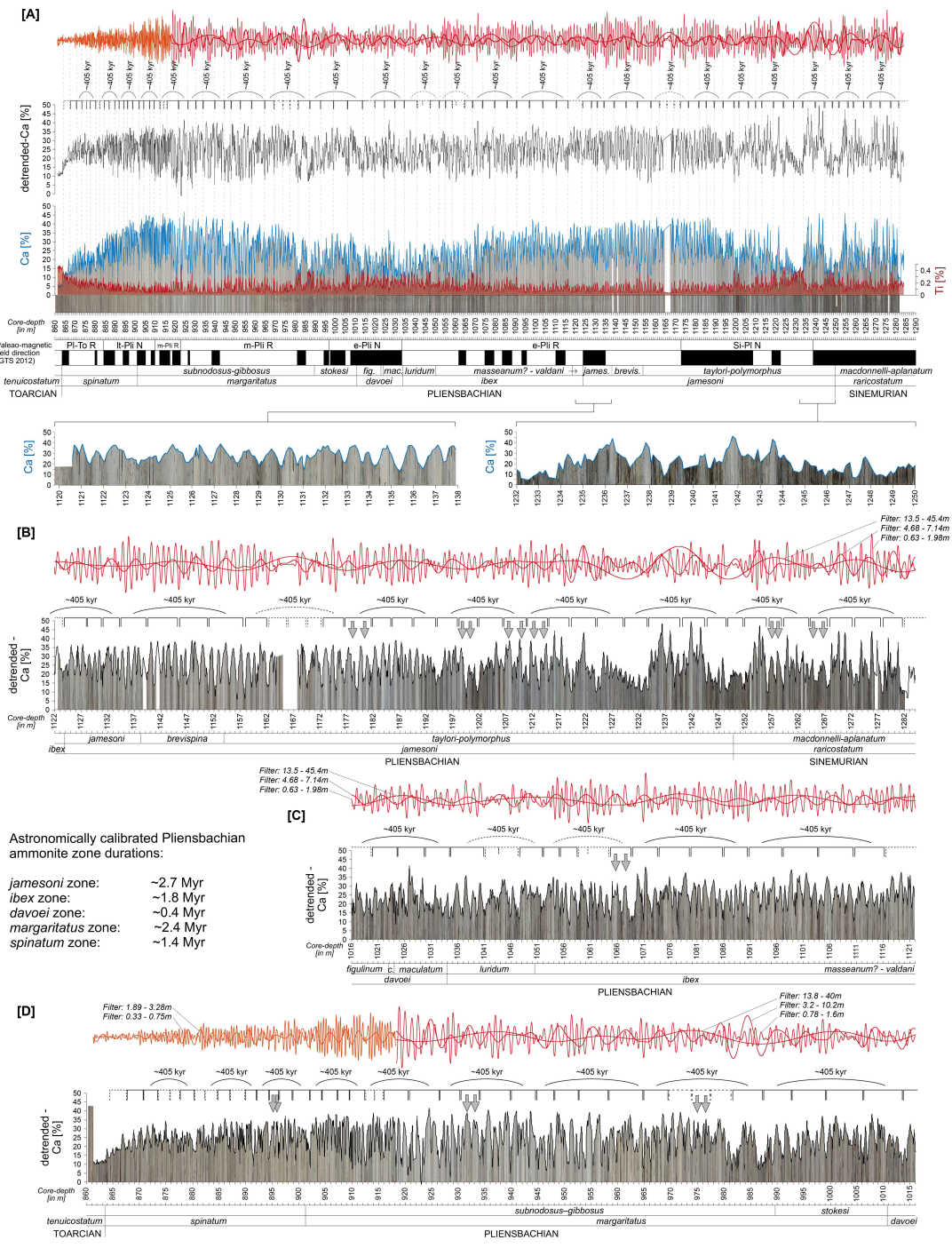


FIGURE 4



Astronomically calibrated Pliensbachian ammonite zone durations:

- jamesoni* zone: ~2.7 Myr
- ibex* zone: ~1.8 Myr
- davoei* zone: ~0.4 Myr
- margaritatus* zone: ~2.4 Myr
- spinatum* zone: ~1.4 Myr

1428
1429
1430
1431
1432
1433
1434
1435
1436
1437
1438
1439
1440
1441
1442
1443
1444
1445
1446
1447
1448
1449
1450
1451
1452
1453
1454
1455
1456
1457
1458
1459
1460
1461
1462
1463
1464
1465
1466
1467
1468
1469
1470
1471
1472
1473
1474
1475
1476
1477
1478
1479
1480
1481
1482
1483

1484
1485
1486
1487
1488
1489
1490
1491
1492
1493
1494
1495
1496
1497
1498
1499
1500
1501
1502
1503
1504
1505
1506
1507
1508
1509
1510
1511
1512
1513
1514
1515
1516
1517
1518
1519
1520
1521
1522
1523
1524
1525
1526
1527
1528
1529
1530
1531
1532
1533
1534
1535
1536
1537
1538
1539

FIGURE 5

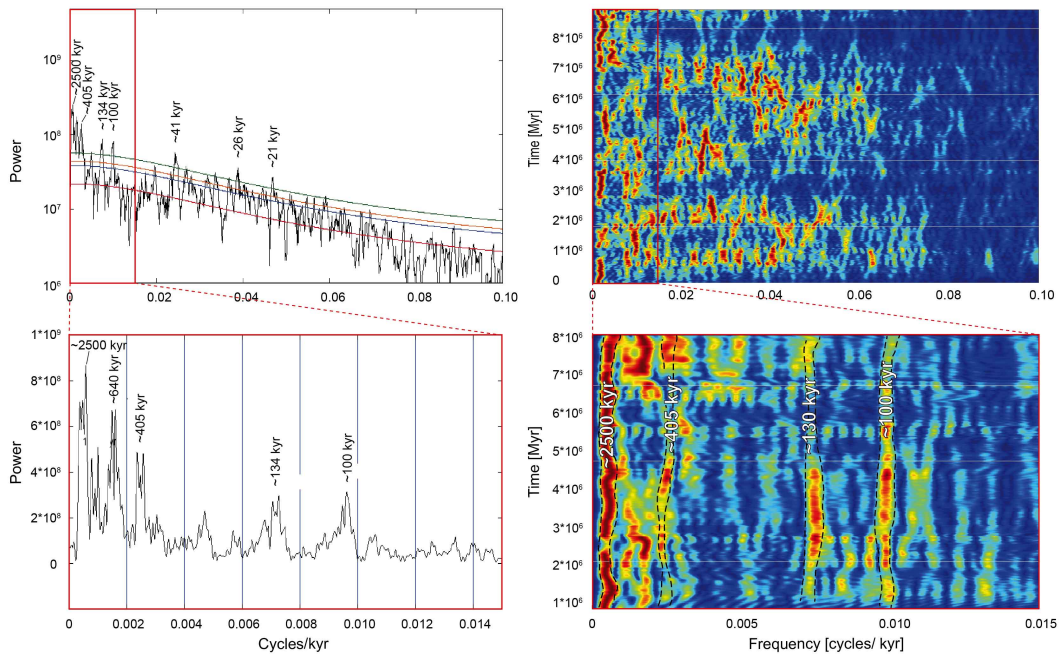
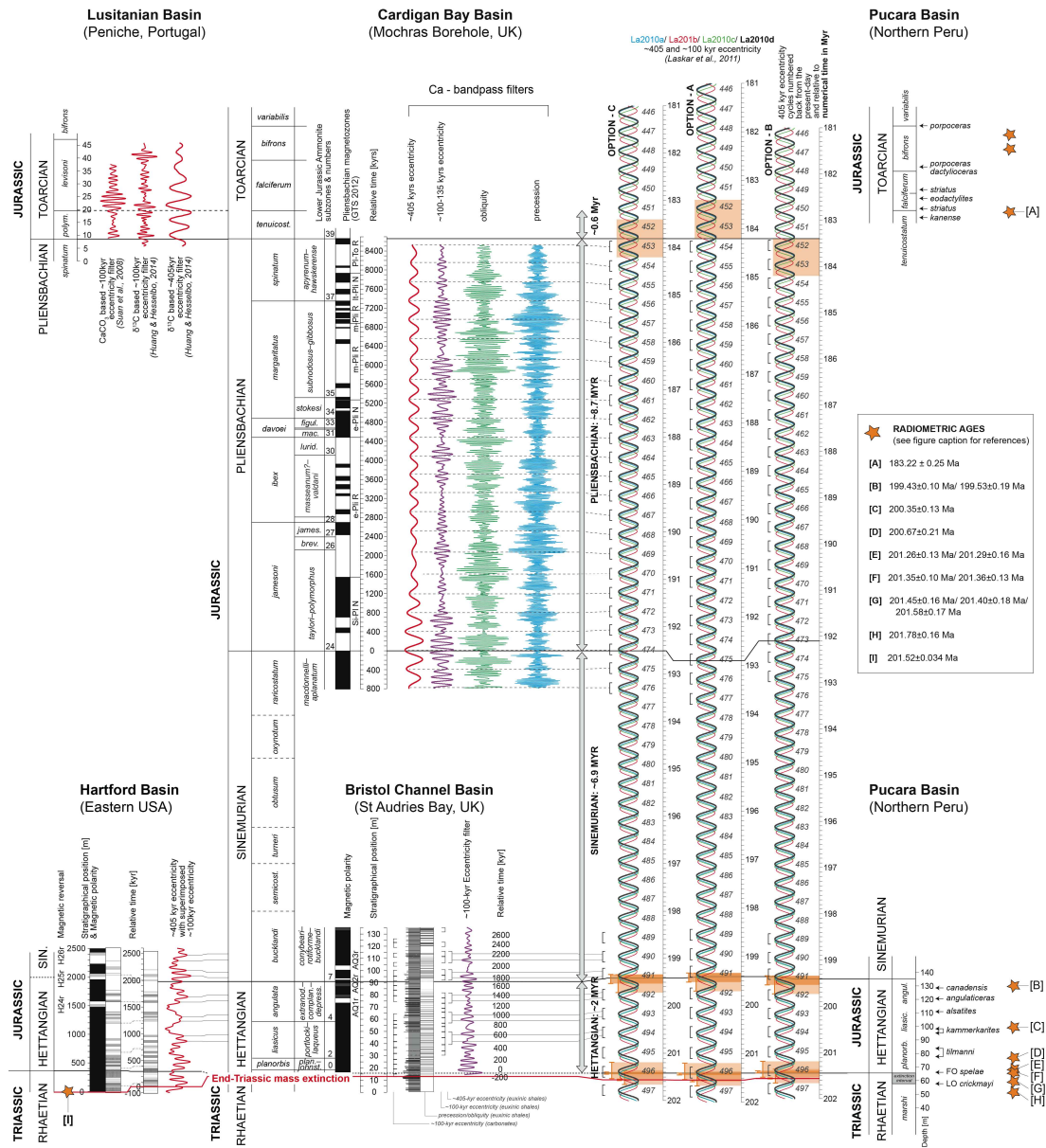


FIGURE 6



1596
1597
1598
1599
1600
1601
1602
1603
1604
1605
1606
1607
1608
1609
1610
1611
1612
1613
1614
1615
1616
1617
1618
1619
1620
1621
1622
1623
1624
1625
1626
1627
1628
1629
1630
1631
1632
1633
1634
1635
1636
1637
1638
1639
1640
1641
1642
1643
1644
1645
1646
1647
1648
1649
1650
1651

FIGURE 7

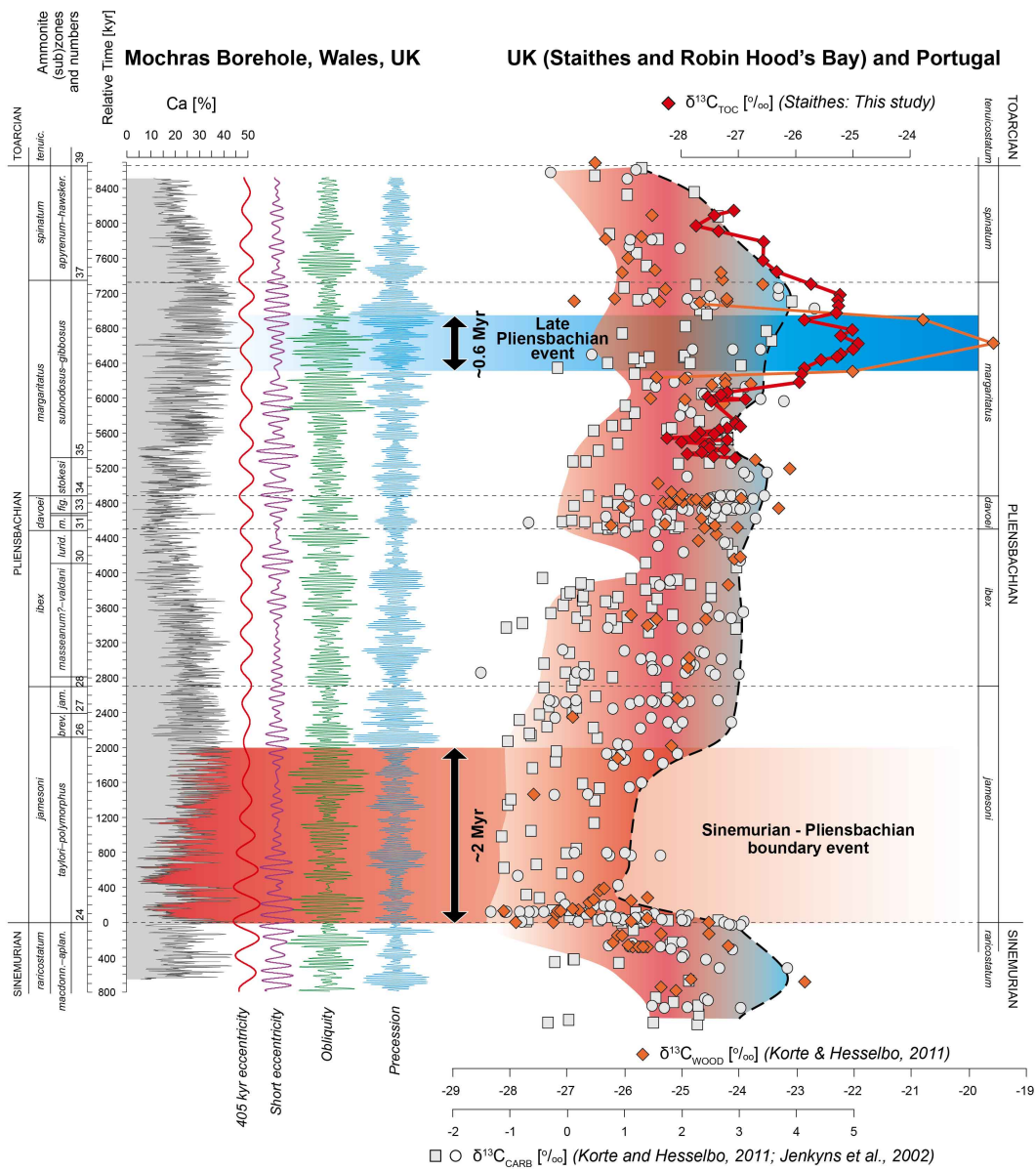
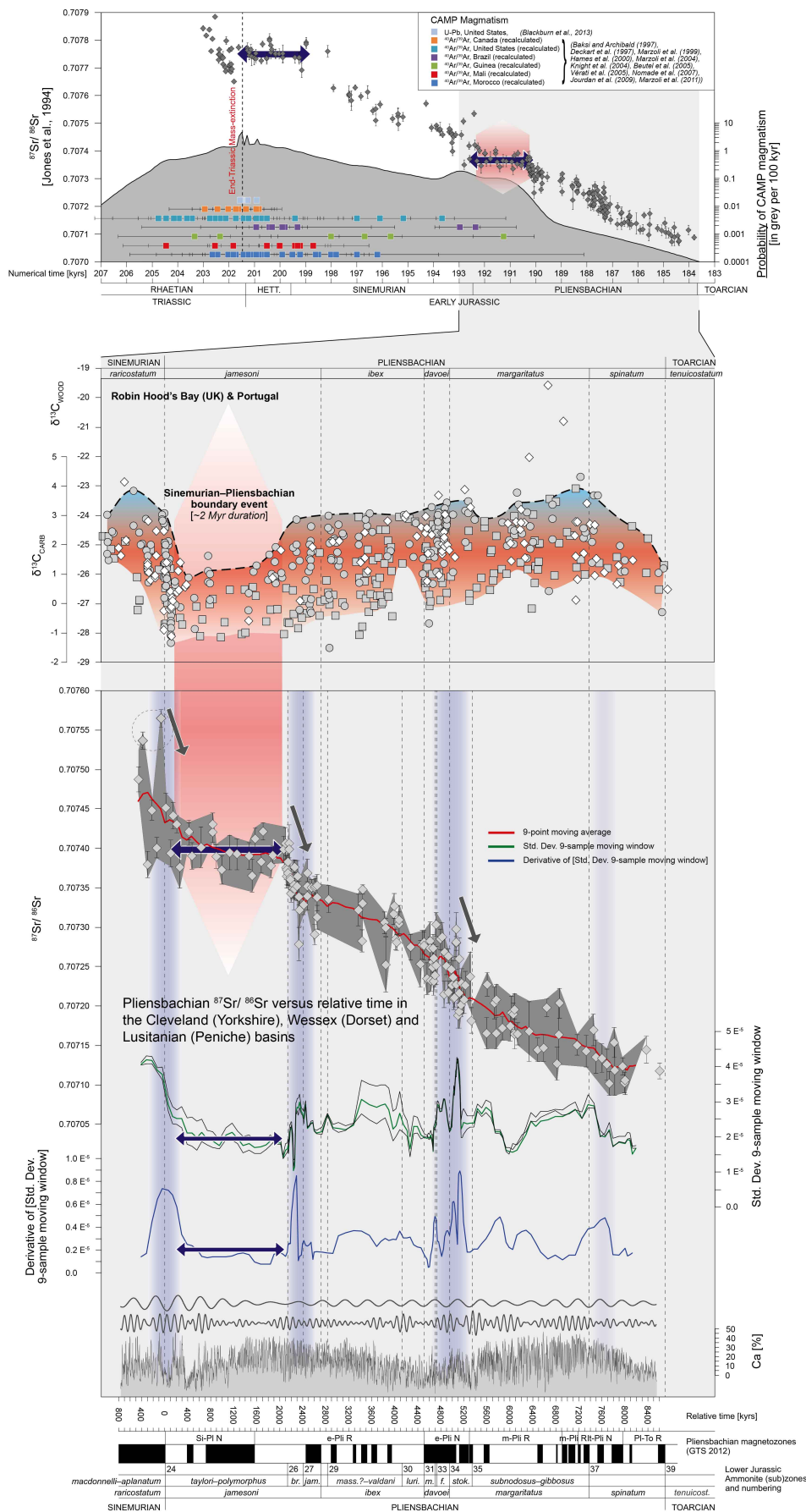


FIGURE 8



1652
1653
1654
1655
1656
1657
1658
1659
1660
1661
1662
1663
1664
1665
1666
1667
1668
1669
1670
1671
1672
1673
1674
1675
1676
1677
1678
1679
1680
1681
1682
1683
1684
1685
1686
1687
1688
1689
1690
1691
1692
1693
1694
1695
1696
1697
1698
1699
1700
1701
1702
1703
1704
1705
1706
1707

1708
 1709
 1710
 1711
 1712
 1713
 1714
 1715
 1716
 1717
 1718
 1719
 1720
 1721
 1722
 1723
 1724
 1725
 1726
 1727
 1728
 1729
 1730
 1731
 1732
 1733
 1734
 1735
 1736
 1737
 1738
 1739
 1740
 1741
 1742
 1743
 1744
 1745
 1746
 1747
 1748
 1749
 1750
 1751
 1752
 1753
 1754
 1755
 1756
 1757
 1758
 1759
 1760
 1761
 1762
 1763

TABLE 1

Table 1: Early Jurassic Stage and ammonite zone ages and durations

Stage	Ammonite Zone	Base Age [Myr]	Base age: radiometric and astrochronological uncertainty [Myr]	Mochras Borehole: base biostratigraphic uncertainty [Myr]	Duration and biostratigraphic uncertainty [Myr]
Toarcian	<i>tenuicostatum</i>	183.8	+/-0.4	+0.25	~0.6
		183.8	+/-0.4 <small>(combined astrochr./radiom. uncertainty)</small>	+0.25	~8.3
	<i>spinatum</i>	185.2	+/-0.4 <small>(extrapolated from above)</small>	+0.25	~1.4 (+0.25/-0.25)
	<i>margaritatus</i>	187.6	+/-0.4 <small>(extrapolated from above)</small>	0	~2.4 (-0.25)
	<i>davoei</i>	188.0	+/-0.4 <small>(extrapolated from above)</small>	0	~0.4
Pliensbachian	<i>ibex</i>	189.8	+/-0.4 <small>(extrapolated from above)</small>	0	~1.8
	<i>jamesoni</i>	192.5	+/-0.4 <small>(extrapolated from above)</small>	+0.15	~2.7 (+0.15)
		192.5	+/-0.4 <small>(extrapolated from above)</small>	+0.15	~8.7 (+0.15/-0.25)
	<i>raricostatum</i>				> 0.8
	<i>oxynotum</i>				
Sinemurian	<i>obtusum</i>				
	<i>turneri</i>				
	<i>semicostatum</i>				
	<i>bucklandi</i>	199.43	+/-0.1 <small>(radiometric uncertainty)</small>		> 1.1
		199.43	+/-0.1 <small>(radiometric uncertainty)</small>		6.93 (+0.75/-0.65)
Hettangian	<i>angulata</i>	~200.25			~0.82
	<i>liasicus</i>	~201.04			~0.79
	<i>planorbis</i>	~201.35			~0.31
	<i>spelae</i>	201.42	+/-0.02 <small>(radiometric uncertainty)</small>		1.99 (+/-0.12)

Supplementary Materials

ASTRONOMICAL CONSTRAINTS ON THE DURATION OF THE EARLY JURASSIC PLIENSBACHIAN STAGE AND GLOBAL CLIMATIC FLUCTUATIONS

*Rubl, M., Hesselbo, S.P., Hinnov, L., Jenkyns, H.C., Xu, W., Riding, J., Storm, M.,
Minisini, D., Ullmann, C.V., Leng, M.J.*

[1] ANALYTICAL METHODS

High-resolution (10–15 cm) elemental concentrations (e.g. Ca, Ti, Fe, Rb, Zr) were obtained by hand-held X-ray fluorescence (XRF) analyses on the slabbed archive half of the Mochras core, from the late Sinemurian *ruricostatum* zone (starting at 1284.08 m in the *macdonnelli–aplanatum* subzone) to the Early Toarcian *tenuicostatum* zone (up to a depth of 861.32 m). XRF analyses were conducted with a Thermo Scientific Niton XLT instrument, with a 50-sec measurement window, in soil mode. Long-term drift in measurement values was counteracted by regular internal calibration. Internal measurement uncertainty, partly due to internal calibration and Compton normalization, differs between elements and is reported in Table 1. Long-term drift in analyses was further checked by repeated analysis of the NIST2780 and NIST2709 international reference standards. Repeated analysis of the NIST2780 standard showed for calcium (Ca) an average of 1426 ppm, with a standard deviation (StDev) of 205 ppm and an average internal error of 112 ppm, and for iron (Fe) an average of 28395 ppm, with a standard deviation of 240 ppm and an average internal error of 216 ppm. Repeated analysis of the NIST2709 standard showed for calcium an average of 21130 ppm, with a standard deviation of 362 ppm and an average internal error of 476 ppm, and for Fe an average of 34678 ppm, with a standard deviation of 382 ppm and an average internal error of 454 ppm. Reproducibility of XRF-based calcium concentration data was further confirmed by comparison to Rock-Eval derived calcium carbonate content (CaCO₃; calculated from mineral carbon) (Supplementary Figure 1).

Rock-Eval analysis was performed with the Rock-Eval VI unit from Vinci Technologies, at the department of Earth Sciences, University of Oxford. Samples were homogenised and ~50 mg of sample was subsequently analysed by heating (with incremental temperature increases from room temperature to up to 850°C) in the oxidation and pyrolysis ovens. Mineral carbon content was calculated from the S3_{MINC} and S5 peaks, resulting from the CO and CO₂ flux from the sample and analysed by infrared detector. The TOC content was simultaneously obtained in the same sample-run and was calculated from the combined CO and CO₂ fluxes representing the Pyrolysable Carbon (PC: S1 + S2 + S3_{CO} + S3_{CO2}) and the Residual Carbon (RC: S4_{CO} + S4_{CO2}). Precision and accuracy of the Rock-Eval analyses was checked by regular measurement of the in-house standard SAB134 (a Lower Jurassic shale) and the international reference standard IFP160000. Repeated long-term analyses of the mineral carbon content of the in-house SAB134 standard shows an average of 5.97%, with a StDev of 0.37%. These values include all outliers; performance is generally better, with an average concentration of 6.03% and a StDev of 0.11%. Repeated long-term analyses of the mineral carbon content of the IFP160000 standard shows an average concentration of 3.20%, with a StDev of

1813 0.02% (the mineral carbon concentration of this standard is referenced at $3.26 \pm 0.12\%$).
1814 Repeated long-term analyses of the TOC content of the in-house SAB134 standard
1815 shows an average of 2.87%, with a StDev of 0.39%. These values include all outliers;
1816 performance is generally better, with an average concentration of 2.80% and a StDev of
1817 0.11%. Repeated long-term analyses of the TOC content of the IFP160000 standard
1818 showed an average concentration of 3.27%, with a StDev of 0.04% (the TOC content of
1819 this standard is referenced at $3.28 \pm 0.14\%$).

1820 Calcium concentration spot-analysis by XRF was performed on the slabbed core,
1821 whereas CaCO₃ analysis (calculated from the mineral carbon content) by Rock Eval was
1822 performed on homogenised 1 cm³ samples from stratigraphically nearby (within a few
1823 cm), but different, depth intervals (Supplementary Figure 1). Despite this minor
1824 stratigraphic offset, calculated calcium concentrations from Rock Eval and adjacent XRF
1825 measurements still correlate well (with $R^2 > 0.75$) (Supplementary Figure 1). Additionally,
1826 minor offsets between the Ca-concentration from XRF analyses and the calculated Ca-
1827 concentration, based on the mineral carbon content measured by Rock-Eval, may also
1828 derive from the presumption that carbonate minerals are all associated with calcite, as
1829 CaCO₃. Some of the carbonate minerals in the host-rock may exist as dolomite or
1830 siderite, rather than calcium carbonate. The combined internal error on XRF-based Ca
1831 analysis and Rock Eval-based CaCO₃ analysis was at any time 1–2 orders of magnitude
1832 smaller than the observed variability between the mudstone/marl and the calcareous
1833 mudstone/limestone in the Mochras core.

1834 Analysis of $\delta^{13}\text{C}_{\text{TOC}}$ was performed on decarbonated and homogenized Upper
1835 Pliensbachian outcrop samples from Staithes (Yorkshire; locality described in Korte and
1836 Hesselbo (2011)). One gram of homogenized sample material was decarbonated twice
1837 with 3 M HCl in a warm water bath at 80 °C for 5 hours. The sample was subsequently
1838 rinsed three times with Milli-Q water to reach neutral pH levels. Between 1–10 mg of
1839 decarbonated sample (aiming for ~25 µg pure carbon) was then weighed into 8×5 mm
1840 thin capsules for $\delta^{13}\text{C}_{\text{TOC}}$ analyses. $\delta^{13}\text{C}_{\text{TOC}}$ analyses were performed at the School of
1841 Archaeology (University of Oxford) and at the Stable Isotope Laboratory at the Open
1842 University (Milton Keynes, UK), with a Thermo Scientific Flash 2000 HT Elemental
1843 Analyser (EA) coupled to a Thermo Scientific MAT253 isotope ratio mass spectrometer
1844 via a ConFlo IV open split interface. The Thermo Scientific Flash 2000 HT EA has a
1845 MAS2000 carousel and, between the carousel and the EA, sits a Thermo No Blank
1846 Device (NBD), allowing for the single sample purging with helium. The EA is also
1847 equipped with a Thermal Conductivity Detector (TCD). Automated dilution of sample
1848 gas with the ConFlo IV open split interface allowed for high dynamic range of C (+N)
1849 content and controlled the introduction of the reference gases. Analytical precision at the
1850 Open University was checked by routine analysis of three internal and referenced
1851 laboratory standards, urea 020914MAG, glutamic acid light and Alanine-A, which give
1852 measured average $\delta^{13}\text{C}$ values of -43.9% , -25.1% and -22.2% , respectively, with
1853 standard deviations of 0.3‰, 0.2‰ and 0.1‰. Analytical precision for $\delta^{13}\text{C}_{\text{TOC}}$ analyses at
1854 the University of Oxford was checked by routine analysis of the Alanine-B international
1855 reference standard, which showed average $\delta^{13}\text{C}_{\text{TOC}}$ of -26.9% , with a StDev of 0.1‰
1856 (the Alanine-B standard is referenced at -26.65%). Isotope ratios are reported in
1857 standard delta notation relative to Vienna PDB.
1858

1859 [2] SUPPLEMENTARY FIGURE CAPTIONS
1860 SUPPLEMENTARY FIGURE 1 Comparison of hand-held X-ray fluorescence
1861 (blue) and Rock Eval-based (red) calcium (Ca) concentrations in a selected part of the
1862 Mochras Core. Note that analyses are not performed on the same stratigraphic sample-
1863 depths. Black dots give the stratigraphic difference in centimetre between a Rock-Eval
1864 measurement and the stratigraphically nearest hand-held XRF analyses. Despite the
1865 Rock-Eval and hand-held XRF analyses on stratigraphically different (but nearby)
1866 samples, the obtained Ca concentrations correlate well, with an R^2 of ~ 0.75 .
1867
1868 SUPPLEMENTARY FIGURE 2 XRF-derived Ca-concentrations across the
1869 Sinemurian-Pliensbachian boundary are plotted on top of the stacked core-photos
1870 showing clear correlation between elevated Ca-concentrations and lighter-grey
1871 sedimentary horizons. Mineral carbon content, derived by Rock-Eval analyses, closely
1872 matches fluctuations in Ca-concentrations. TOC and HI values, derived from Rock-Eval
1873 analyses negatively correlate to Ca and mineral-carbon concentrations.
1874
1875 SUPPLEMENTARY FIGURE 3 Scanning Electron Microscopy (SEM) backscatter
1876 pictures of (A) a calcareous mudstone (depth: 842.04 m core-depth below surface) with
1877 fine silt-sized detrital calcite grains circled in red dashed line and (B) a limestone interval
1878 (depth: 807.19 m core-depth below surface), with a massive calcium carbonate matrix
1879 and some replacement by quartz.
1880
1881 SUPPLEMENTARY FIGURE 4 Multi-taper (MTM) spectral analyses of the
1882 obtained XRF elemental (Ca) depth series using the Astrochron (R (3.1.2) Package for
1883 astrochronology, version 0.3.1) toolkit (Meyers, 2014). (A) Multi-taper (MTM) power
1884 spectrum of the complete Pliensbachian (uppermost *rivicostatum* to lowermost
1885 *tenuicostatum*) Ca record, showing clear dominance of the >150 m periodicity. (B) Multi-
1886 taper (MTM) power spectrum of the complete detrended (high band-pass filter
1887 <150 m)) Pliensbachian (uppermost *rivicostatum* to lowermost *tenuicostatum*) Ca-record.
1888 (C) Multi-taper (MTM) power spectrum of the detrended (high band-pass filter
1889 <150 m)) uppermost *rivicostatum* to lower *margaritatus* Ca-record. (D) Multi-taper (MTM)
1890 power spectrum of the detrended (high band-pass filter <150 m)) upper *margaritatus* to
1891 lowermost *tenuicostatum* Ca record. Note the order of magnitude differences in Linear
1892 Power for the MTM Power estimates, especially for Figure D.
1893
1894 SUPPLEMENTARY FIGURE 5 Multi-taper (MTM; 3π) spectral analyses of the
1895 obtained XRF elemental (Fe and Ca) time series using the Astrochron (R (3.1.2) Package
1896 for astrochronology, version 0.3.1) toolkit (Meyers, 2014), with robust red noise models
1897 (Mann and Lees, 1996). The elemental Fe record was first manipulated to give uniform
1898 sample spacing using linear interpolation. Initial spectral analysis was performed with
1899 AnalySeries on a detrended data-series (with low band-pass filtering to remove >150 m
1900 periodicities). Dominant spectral components (Supplementary Figure 3) were
1901 subsequently filtered from the data series and compared to the visually defined
1902 precession and short- and long-eccentricity periodicities (Figure 3). The elemental Ca
1903 record in the depth domain was subsequently converted to the time domain following
1904 the observed 405 kyr eccentricity cycles. The multi-taper (MTM; 3π) spectral analyses of
1905 the obtained elemental (Fe and Ca) time-series show dominant and significant peaks at
1906 precession, obliquity, and short- and long-period eccentricity. MTM power estimates,
1907 AR1 confidence level estimates and harmonic test confidence level estimates are
1908 performed with the Astrochron (R (3.1.2) Package for astrochronology, version 0.3.1)
1909 toolkit (Meyers, 2014). An independent check of the dominant spectral components is

1910 performed with AnalySeries 2.0.8 (Paillard et al., 1996), giving a 80% confidence interval
1911 (grey).

1912
1913 SUPPLEMENTARY FIGURE 6 Precession (blue), obliquity (green), 100–135 kyr
1914 eccentricity (purple) and 405 kyr eccentricity (red) band-pass filters, reflecting frequency
1915 intervals in the MTM power spectra (Supplementary Figure 4) of the detrended (high
1916 band-pass) Fe and Ca time series.

1917
1918 SUPPLEMENTARY FIGURE 7 Comparison of the Pliensbachian stratigraphic
1919 depth record with the obtained Pliensbachian time series shows a pronounced 40–60%
1920 decrease in sedimentation rate in the upper *margaritatus* ammonite zone (starting at
1921 ~918m core depth). Lower Jurassic (top Sinemurian to base Toarcian) ammonite genera
1922 occurrence is based on Woodland (1971). Blue bars represent the occurrence of
1923 ammonite genera, with a specific genus occurring within a 20 feet (6.096m) window
1924 (Woodland, 1971). Minor refinements on ammonite zone boundary positions are based
1925 on Copestake and Johnson (2014), which are followed here. Many ammonite (sub)zone
1926 boundaries are constrained by first and last occurrences of ammonite genera. Some
1927 (sub)zone boundaries are potentially less well constrained, as recognized by a grey bar.

1928
1929 SUPPLEMENTARY FIGURE 8 Lower Pliensbachian (*jamesoni* ammonite zone)
1930 $^{87}\text{Sr}/^{86}\text{Sr}$ data plotted in time in kyrs, (A) based on the Mochras-core derived
1931 Pliensbachian time-scale as presented in Figure 8 of the main-text, (B) based on the
1932 Belemnite Marls (Dorste, UK) derived Lower Pliensbachian time-scale as presented in
1933 Weedon and Jenkyns (1999), and (C) assuming equal duration of Pliensbachian
1934 ammonite zones. The Early Pliensbachian $^{87}\text{Sr}/^{86}\text{Sr}$ record in the time-domain shows a
1935 plateau, with relatively constant values, throughout the *taylori-polymorphus* ammonite
1936 subzones, followed by a rapid drop in the *brevispina* ammonite subzone, based on both
1937 the Mochras and the Belemnite Marl derived time-scales. (D) MTM Power spectrum of
1938 the tuned *jamesoni*-ammonite zone % Ca-record of the Mochras core, based on the
1939 Mochras-time-scale (this study), and (E) the tuned *jamesoni*-ammonite zone % Ca-record
1940 of the Mochras core, based on the Belemnite Marl time-scale of Weedon and Jenkyns
1941 (1999), following similar methods and parameters as presented in Supplementary Figures
1942 4 and 5. (D) Clear peaks on expected astronomical frequencies, while peaks in (E) show
1943 no resemblance to astronomical frequencies as known from the geological record and
1944 astronomical solutions. This inconsistency suggests that the Lower Pliensbachian time-
1945 scale based on the Belemnite Marls is incorrect, which can be largely explained by the
1946 observed sedimentary hiatuses at the base of the *jamesoni* ammonite subzone and
1947 possibly within the *brevispina* ammonite subzone.

1948
1949 [3] REFERENCES

- 1950 Cope, J.C.W., Getty, T.A., Howarth, M.K., Morton, N., Torrens, H.S., A correlation of Jurassic
1951 rocks in the British Isles, Part One: Introduction and Lower Jurassic. Geol. Soc. Lond.,
1952 Special report No. 14 (1980).
- 1953 Copestake, P., Johnson, B., Lower Jurassic Foraminifera from the Llanbedr (Mochrad Farm)
1954 Borehole, North Wales, UK. Monograph of the Palaeontographical Society, London: 1–
1955 403 (2014).
- 1956 Ivimey-Cook, H.C., Stratigraphical Palaeontology of the Lower Jurassic of the Llanbedr
1957 (Mochras Farm) Borehole. In: Woodland, A.W. (Ed). The Llanbedr (Mochras Farm)
1958 Borehole. Institute of Geological Sciences Report No. 71/18, p. 87–92 (1971).
- 1959 Lorenz, J., Gely, J.-P., Interpretation sequentielle du Jurassique Inferieur et moyen du sud du
1960 Basin Parisien a partir des correlations diagraphiques cales sur le forage de Couy (Cher,
1961 France). Geobios 17, p. 597–604 (1994).

1962 Ainsworth, N.R., Riley, L.A., Triassic to Middle Jurassic stratigraphy of the Kerr McGee 97/12-1
1963 exploration well, offshore southern England. *Marine and Petroleum Geology* 27, p. 853–
1964 894 (2010).

1965 Brigaud, B., Vincent, B., Carpentier, C., Robin, C., Guillocheau, F., Yven, B., Huret, E., Growth
1966 and demise of the Jurassic carbonate platform in the intracratonic Paris Basin (France):
1967 Interplay of climate change, eustasy and tectonics. *Marine and Petroleum Geology* 53, p.
1968 3–29 (2014).

1969 Mattioli, E., Plancq, J., Boussaha, M., Duarte, L.V., Pittet, B., Calcareous nannofossil
1970 biostratigraphy: new data from the Lower Jurassic of the Lusitanian Basin. *Comunicacoes*
1971 *Geologicas* 100, p. 69–76 (2013).

1972 Ivimey-Cook, H.C., Biostratigraphy of the Lower Jurassic and Upper Triassic (Rhaetian) rocks of
1973 the Winterborne Kingston borehole, Dorset. Report of the Institute of Geological
1974 Sciences (1982).

1975 Weedon, G.P., Jenkyns, H.C., Cyclostratigraphy and the Early Jurassic timescale: Data from the
1976 Belemnite Marls, Dorset, southern England. *Geological Society of America Bulletin* 111,
1977 p. 1823–1840 (1999).

1978 Whittaker, A., Green, G.W., Geology of the country around Weston-super-Mare. *Mem. Geol.*
1979 *Surv. G.B.* (1983).

1980 Woodland, A.W. (Editor). 1971. The Llanbedr (Mochras Farm) Borehole. Rep. No. 71/18, Inst.
1981 geol. Sci. 115 pp.

1982 Meyers, S.R. (2014), *Astrochron: An R Package for Astrochronology* (Version 0.3.1).

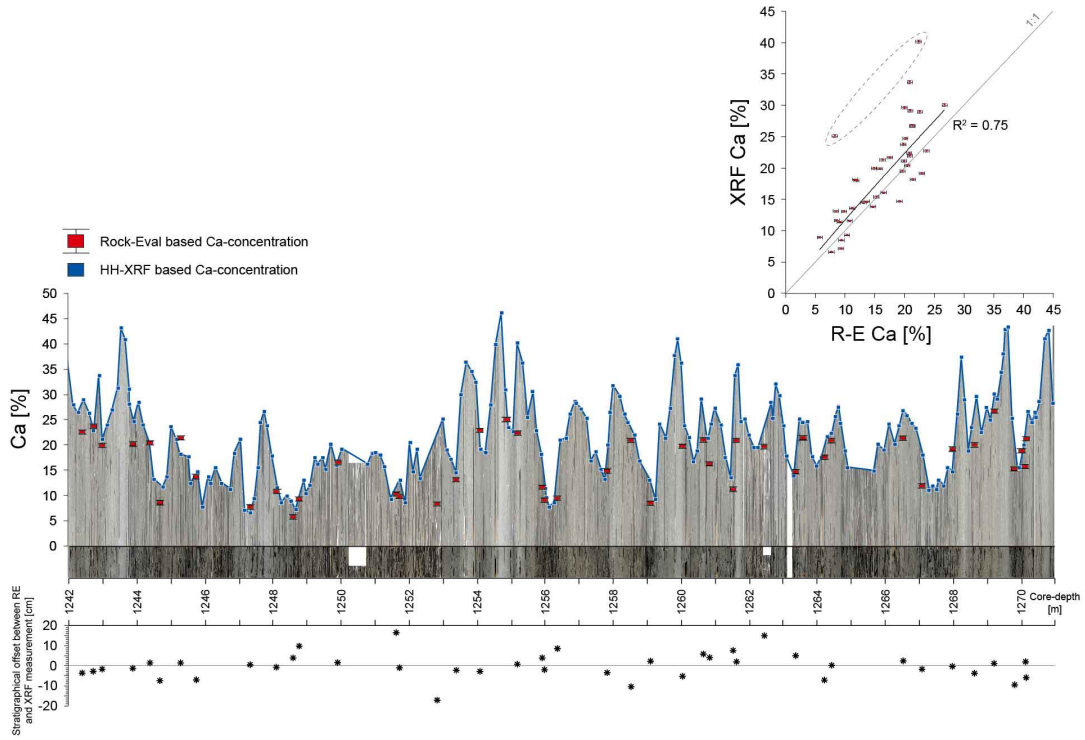
1983 Mann, M.E., Lees, J.M., Robust estimation of background noise and signal detection in climatic
1984 time series. *Climatic Change* 33, p. 409–445 (1996).

1985 Paillard, D., L. Labeyrie and P. Yiou, Macintosh program performs time-series analysis, *Eos*
1986 *Trans. AGU*, 77: 379 (1996).

1987
1988
1989
1990
1991
1992
1993
1994
1995
1996
1997
1998
1999
2000
2001
2002
2003
2004
2005
2006
2007
2008
2009
2010
2011
2012
2013
2014
2015
2016
2017

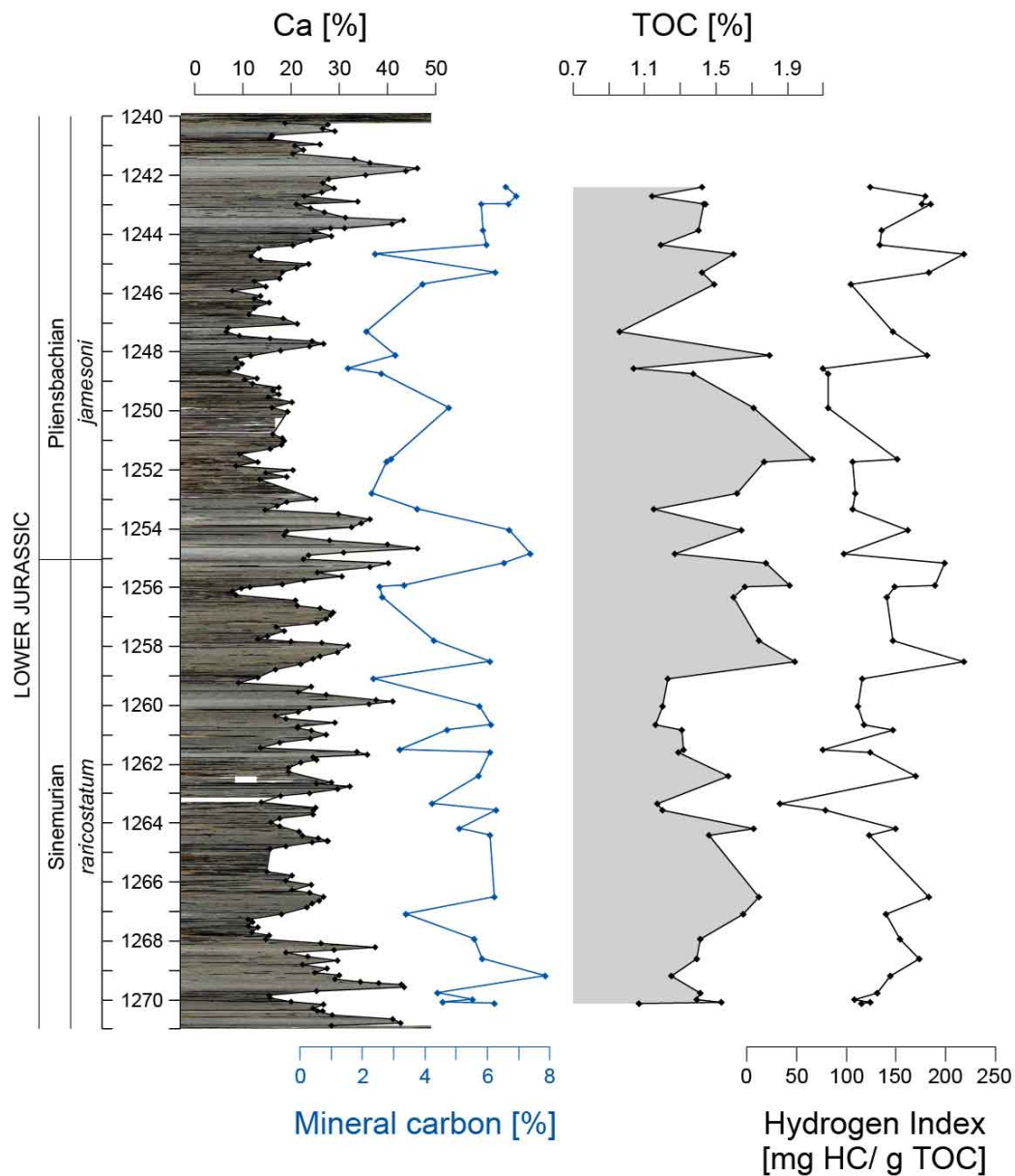
2018
2019
2020
2021
2022
2023
2024
2025
2026
2027
2028
2029
2030
2031
2032
2033
2034
2035
2036
2037
2038
2039
2040
2041
2042
2043
2044
2045
2046
2047
2048
2049
2050
2051
2052
2053
2054
2055
2056
2057
2058
2059
2060
2061
2062
2063
2064
2065
2066
2067
2068
2069
2070
2071
2072
2073

SUPPLEMENTARY FIGURE 1



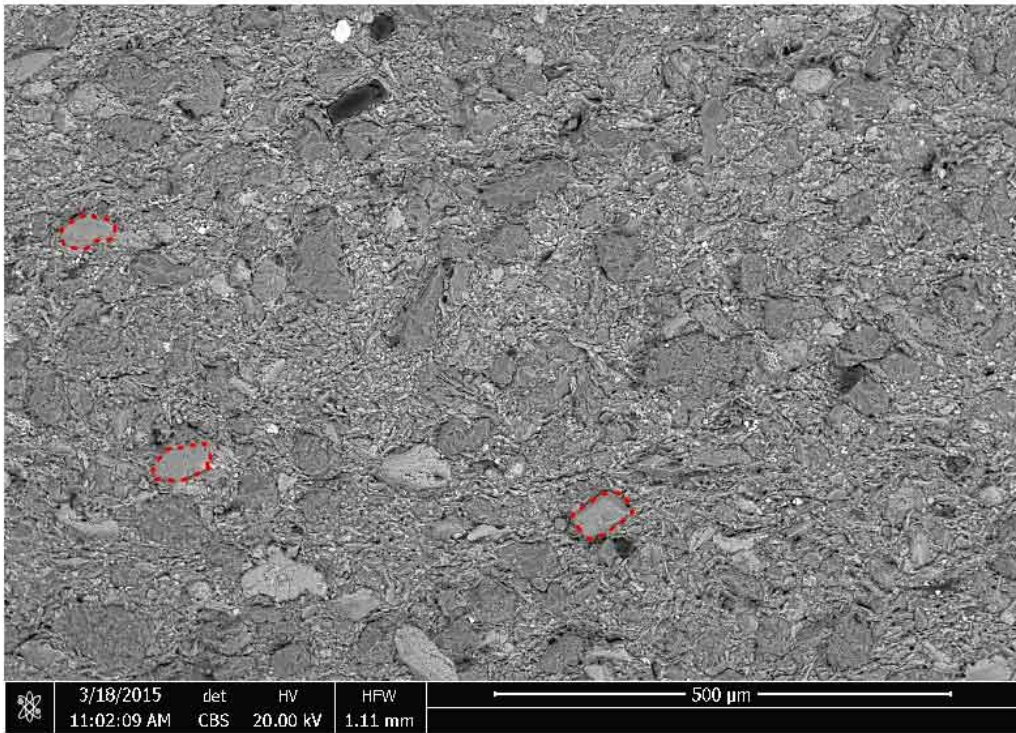
2074
2075
2076
2077
2078
2079
2080
2081
2082
2083
2084
2085
2086
2087
2088
2089
2090
2091
2092
2093
2094
2095
2096
2097
2098
2099
2100
2101
2102
2103
2104
2105
2106
2107
2108
2109
2110
2111
2112
2113
2114
2115
2116
2117
2118
2119
2120
2121
2122
2123
2124
2125
2126
2127
2128
2129

SUPPLEMENTARY FIGURE 2

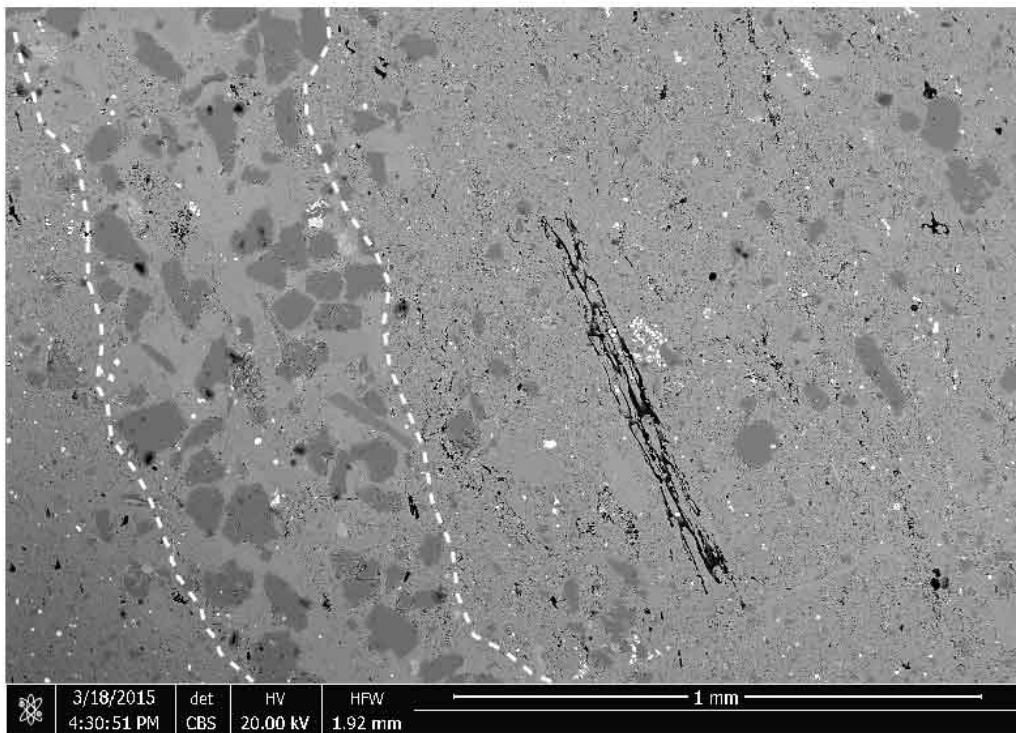


SUPPLEMENTARY FIGURE 3

2130
2131
2132
2133
2134
2135
2136
2137
2138
2139
2140
2141
2142
2143
2144
2145
2146
2147
2148
2149
2150
2151
2152
2153
2154
2155
2156
2157
2158
2159
2160
2161
2162
2163
2164
2165
2166
2167
2168
2169
2170
2171
2172
2173
2174
2175
2176
2177
2178
2179
2180
2181
2182
2183
2184
2185



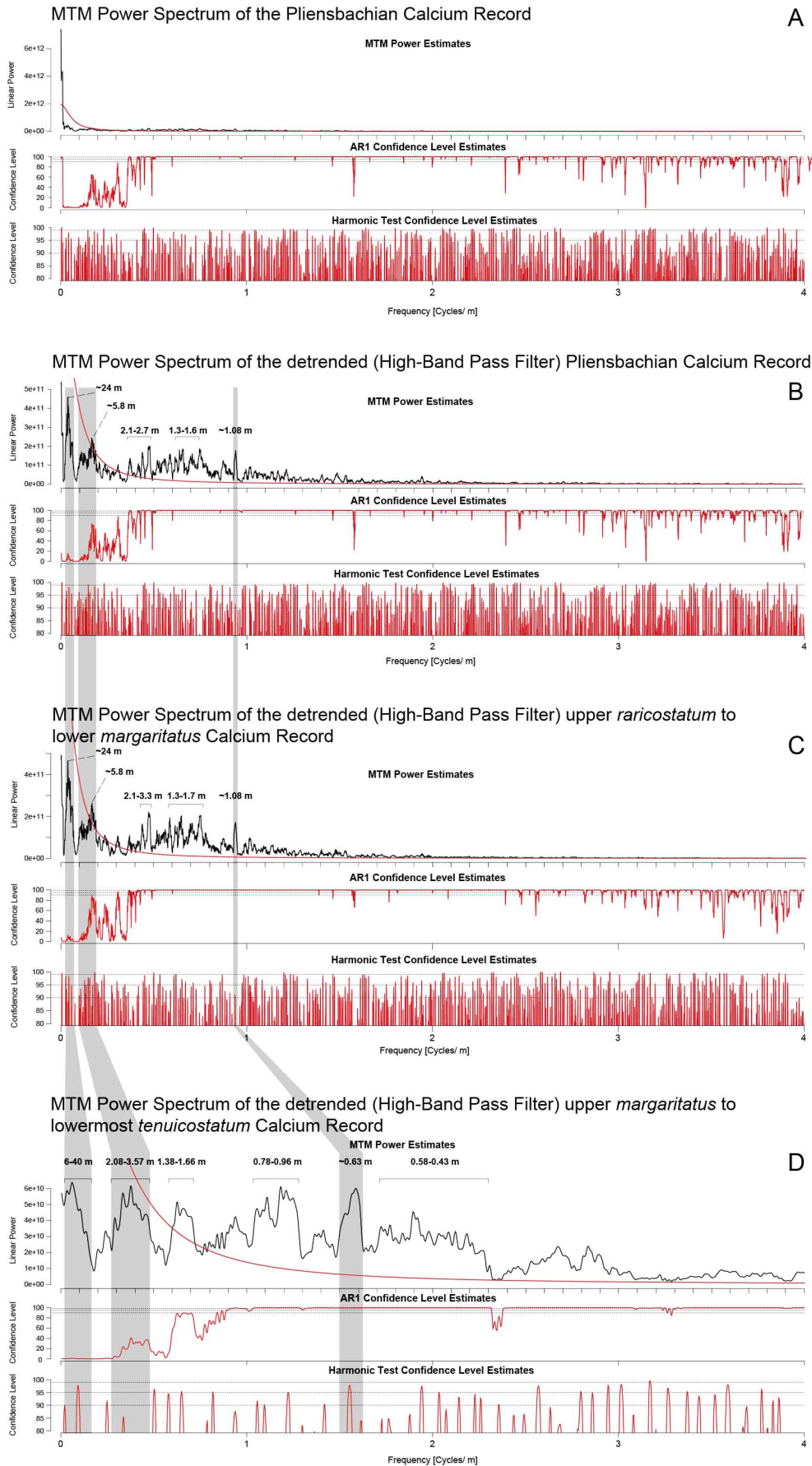
A: Fine silty sized detrital calcite grains circled in red dashed line



B: Fossil-shell fragment (marked by the white dashed line), which is partly replaced by quartz. The shell fragment and a woody clast (in black) are embedded in a likely early diagenetic massive calcium carbonate matrix.

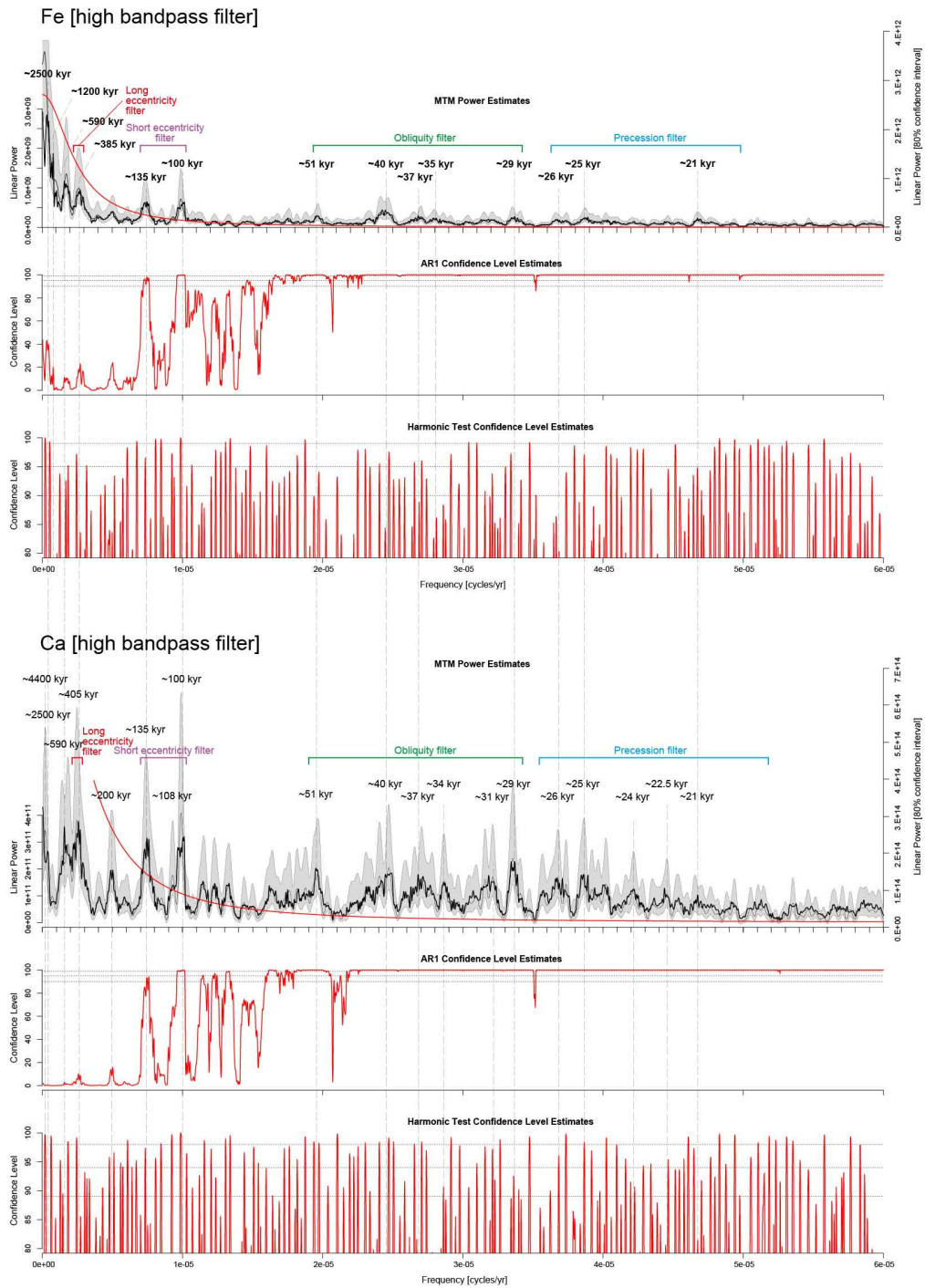
2186
2187
2188
2189
2190
2191
2192
2193
2194
2195
2196
2197
2198
2199
2200
2201
2202
2203
2204
2205
2206
2207
2208
2209
2210
2211
2212
2213
2214
2215
2216
2217
2218
2219
2220
2221
2222
2223
2224
2225
2226
2227
2228
2229
2230
2231
2232
2233
2234
2235
2236
2237
2238
2239
2240
2241

SUPPLEMENTARY FIGURE 4

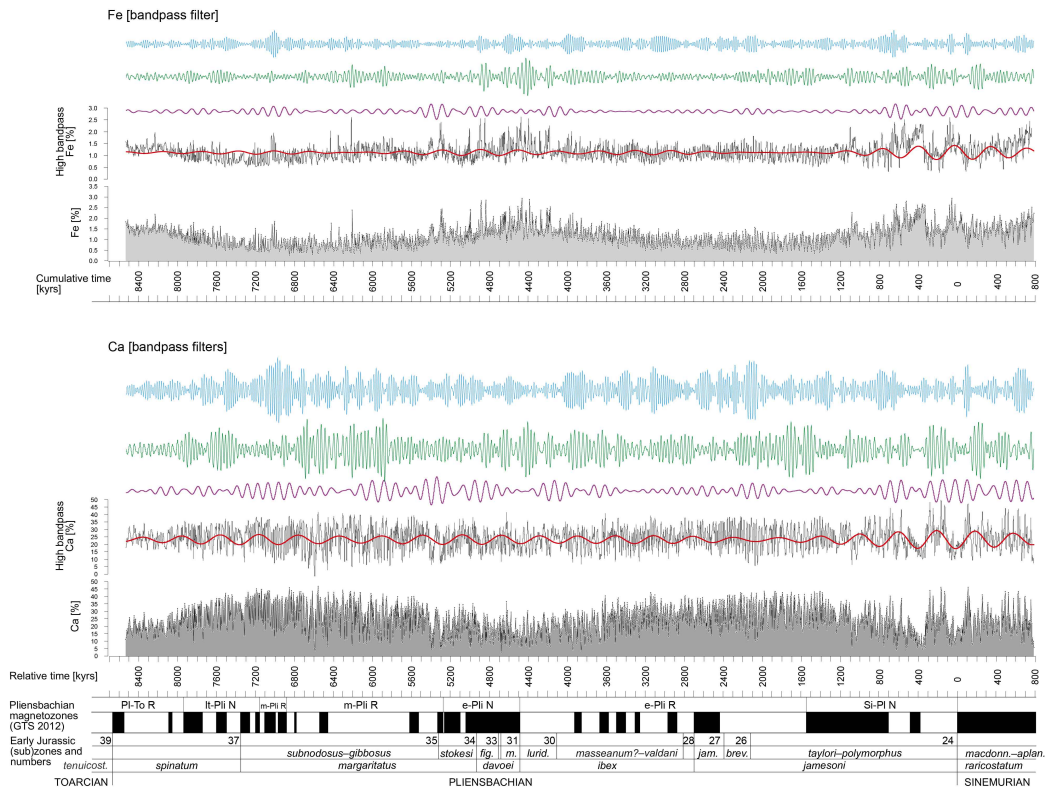


SUPPLEMENTARY FIGURE 5

2242
2243
2244
2245
2246
2247
2248
2249
2250
2251
2252
2253
2254
2255
2256
2257
2258
2259
2260
2261
2262
2263
2264
2265
2266
2267
2268
2269
2270
2271
2272
2273
2274
2275
2276
2277
2278
2279
2280
2281
2282
2283
2284
2285
2286
2287
2288
2289
2290
2291
2292
2293
2294
2295
2296
2297



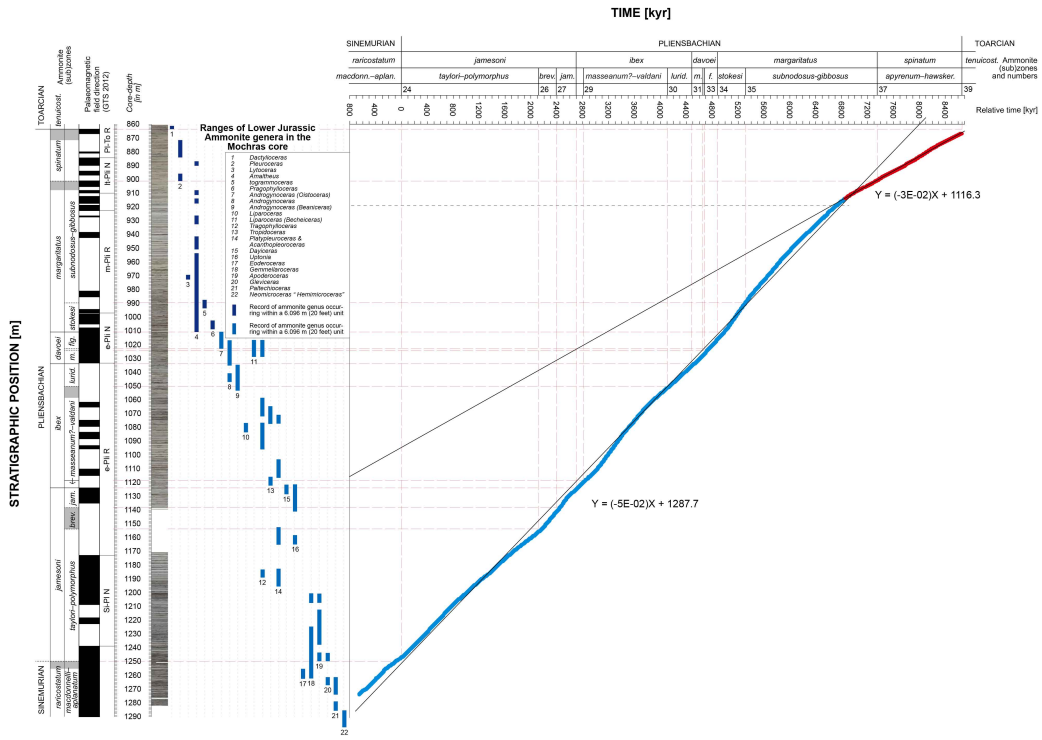
SUPPLEMENTARY FIGURE 6



2298
2299
2300
2301
2302
2303
2304
2305
2306
2307
2308
2309
2310
2311
2312
2313
2314
2315
2316
2317
2318
2319
2320
2321
2322
2323
2324
2325
2326
2327
2328
2329
2330
2331
2332
2333
2334
2335
2336
2337
2338
2339
2340
2341
2342
2343
2344
2345
2346
2347
2348
2349
2350
2351
2352
2353

2354
2355
2356
2357
2358
2359
2360
2361
2362
2363
2364
2365
2366
2367
2368
2369
2370
2371
2372
2373
2374
2375
2376
2377
2378
2379
2380
2381
2382
2383
2384
2385
2386
2387
2388
2389
2390
2391
2392
2393
2394
2395
2396
2397
2398
2399
2400
2401
2402
2403
2404
2405
2406
2407
2408
2409

SUPPLEMENTARY FIGURE 7



SUPPLEMENTARY FIGURE 8

